Structural Defects Modulate Electronic and Nanomechanical Properties of 2D Materials

Manoj Tripathi,*,‡ Frank Lee,‡ Antonios Michail, Dimitris Anestopoulos, James G. McHugh, Sean P. Ogilvie, Matthew J. Large, Aline Amorim Graf, Peter J. Lynch, John Parthenios, Konstantinos Papagelis, Soumyabrata Roy, M. A. S. R. Saadi, Muhammad M. Rahman, Nicola Maria Pugno, Alice A. K. King, Pulickel M. Ajayan,* and Alan B. Dalton*

The intriguing electrical, optical, and mechanical properties of 2D materials offer endless possibilities for high-performance devices. For instance, the virtue of electrons in graphene (Gr) as 2D Dirac Fermions can be employed in supercapacitors[1] and photonic devices.[2] Also, in transition-metal dichalcogenide (TMD) structures such as molybdenum disulfide (MoS_2), the transition from indirect to direct bandgap facilitates the fabrication of biosensors and optoelectronic devices.[3] To optimize device performance, single- to few-layer material is often required, which is conventionally attained by mechanical exfoliation (ME) or chemical vapor deposition (CVD) techniques.

The preparation techniques arise not perfect and inevitably results in a range of structural defects. Mechanical exfoliation

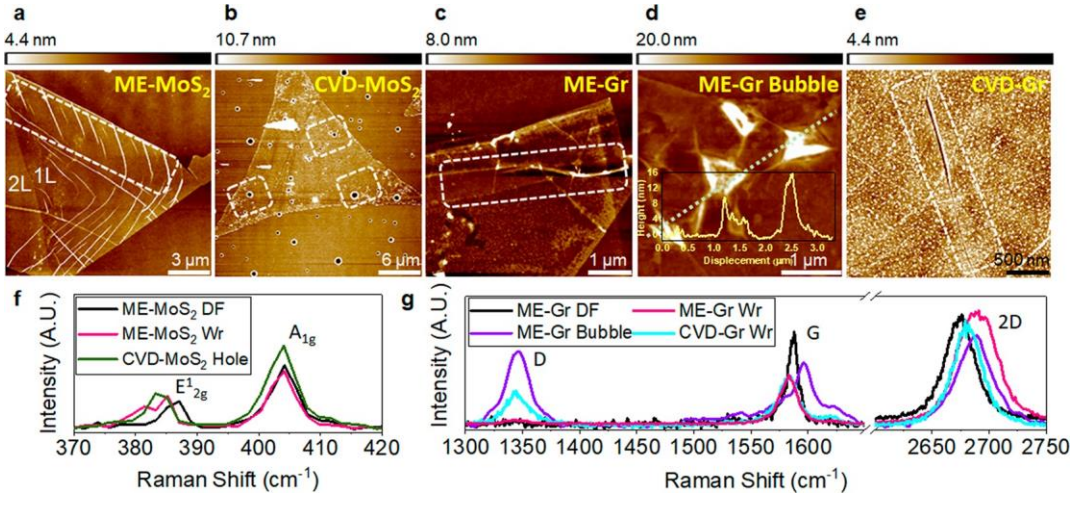

Figure 1. AFM topography and Raman mapping of the structural defects in MoS_2 and Gr. (a) AFM morphology of wrinkled ME-MoS_2, (b) pit-holes in CVD MoS_2, (c) wrinkle in ME-Gr, (d) deflated Gr nanobubble with height ranging from 4 to 16 nm, and (e) grain boundary in CVD-Gr on silica. The dashed rectangle represents the example of structural defect. All color scales shown are relative to zero height. (f, g) Raman spectra of MoS_2 and Gr samples. The presence of defects shifts the active Raman modes: E^1_{2g}, A_{1g} in MoS_2 and G, 2D modes in Gr.

edge, which alters local electronic (surface potential) and mechanical properties of the 2D materials.[6] On the other hand, CVD often generates wrinkles and grain boundaries which originate from the polycrystalline nature of the monolayer and decrease the conductivity of graphene, for instance, by a factor of approximately three.[7] Both fabrication methods followed by a transfer procedure induce wrinkles or nanobubbles owing to thermodynamic instability in 2D sheets[8] and the difference in thermal expansion coefficient (TEC) between the 2D material and the substrate in CVD procedures.[9]

Peculiar properties emerge due to the lattice distortion in wrinkles, which can alter the surface area, conductivity, and molecular resonance states.[4,7,8] While these changes are generally regarded as imperfections, they could possibly create opportunities for flexible devices and nanoelectronics.[10] A comprehensive investigation into the modulation of electronic and nanomechanical properties is therefore essential to elucidate the constraints of each defect which can be considered during device design or exploited for potential applications. Mechanical strain is an important quantifiable property, which is responsible for Dirac cone shifting and Landau quantization in graphene[11] as well as bandgap widening in MoS_2.[12] Understanding the relationship between each type of structural defect and its associated strain is, therefore, critical to advances in the fields of optoelectronics and straintronics where strain engineering could lead to nextgeneration devices.[13]

Traditionally, the strain in 2D materials can be measured and evaluated experimentally by atomic force microscopy (AFM)[14] or theoretically by elastic theories.[15] The former method gives nanometre resolution but fails to quantify relatively small strain on pristine 2D flakes, while the latter is able to estimate small strain but is incapable of assessing complex structures.[16] Thus,

it is imperative to use an alternative and coupled experimental-numerical methodology to examine the minimal strain in nanoscale defects. Another crucial characteristic is doping, which represents the density of charge carriers n that shift the Fermi level and is found to be associated with electron−phonon coupling.[17] It has a compelling contribution for fundamental research; for instance, tuning the electron density can convert graphene into a superconductor,[18] and therefore, an insight into defect-induced doping is vital.

Pioneering work was undertaken by Lee and co-workers,[19] who developed a noninvasive strain and doping evaluation method for graphene at the nanoscale by Raman spectroscopy through correlation between shifts of the G (∼1585 cm^{-1}) and 2D (∼2680 cm^{-1}) modes. Under lateral compression
(tension), the reduction (increase) in the interatomic distances leads to phonon stiffening (softening), and thus, a blue (red) shift of both peaks is observed.[20] Chemical bond modification by static charges and nonadiabatic coupling also shifts the peaks independently of strain.[19,21] Hence, strain and doping can be regarded as two fundamental phenomena which are related to the Raman shift of G and 2D peaks, Pos(G) and Pos(2D), by a linear transformation, and can be determined using a correlation plot of Pos(G) and Pos(2D).[19] The strain and doping in MoS_2 can also be quantitatively determined by the shift of its distinctive E^1_{2g} (∼385 cm^{-1}) and A_{1g} (∼403 cm^{-1}) modes representing the first-order Raman in-plane and out-of-plane phonon modes, respectively.[22,23] Correlation analysis of the Raman shift of E^1_{2g} and A_{1g} peaks, Pos(E^1_{2g}) and Pos(A_{1g}), has enabled numerous studies to examine the in^{fl}uence of ripples,[24,25] curvature,[26] heterostructures,[27] stacking, and domain size.[28]

Nevertheless, Raman studies alone are insufficient for characterization of intrinsic defects due to limited spatial resolution. We thereby implement this compelling approach in combination with AFM studies of structural defects. Thus, information regarding doping, strain, and mechanical stiffness (i.e., resistance to deformation) originating from the structural defects can be obtained, which is critical to fabrication of nanomechanical devices. This approach of extracting mechanical properties from AFM and mechanical strain and electronic doping from Raman mapping has previously only been applied to manipulated crumples,[29] which provides us with motivation in examining the inherent structural defects by this noninvasive technique.

In the present work, we identified common structural defects in mechanically exfoliated MoS_2 (ME-MoS_2), CVD-grown MoS_2 (CVD-MoS_2), mechanically exfoliated graphene (MEGr), and CVD-grown graphene (CVD-Gr) by AFM and scanning electron microscope (SEM). Raman mapping was performed at the defective region along with the surrounding defect-free (DF)

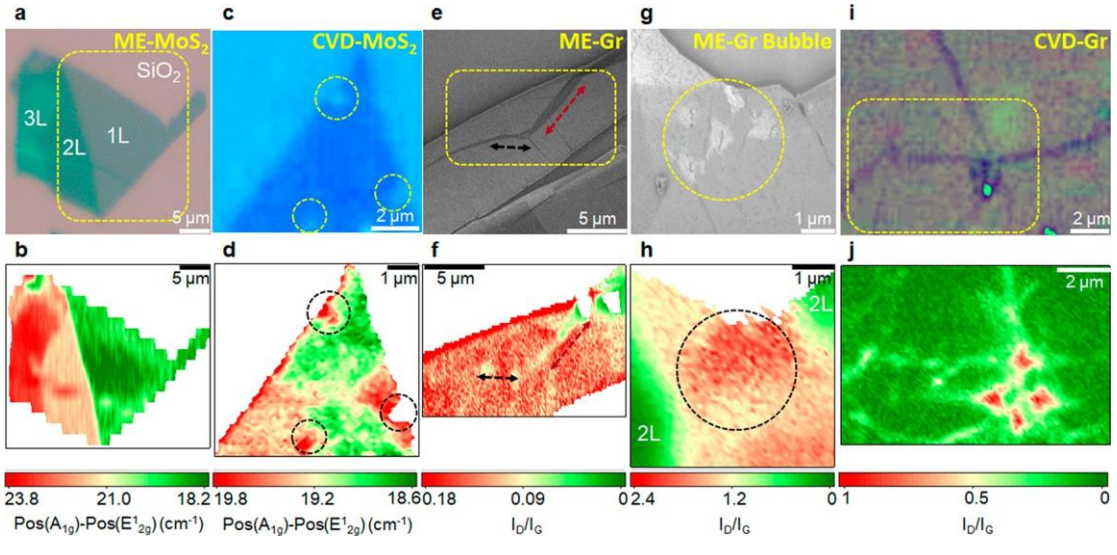

Figure 2. (a−d) Raman mapping of ME-MoS_2 and CVD-MoS_2. The marked region represents the structural defects as wrinkles in ME-MoS_2 and pit-holes in CVD-MoS_2. (e, f) Raman mapping of ME-Gr structural defects; SEM micrograph and the I_D/I_G peak intensity ratio of two different types of wrinkles in ME-Gr as standing collapsed (marked by black color) and transitional-folded wrinkle (marked by red color). (g, h) SEM micrograph and the Raman map of I_D/I_G intensity ratio of six graphene nanobubbles of different geometry and height marked by dashed line circle. (i, j) Optical image and I_D/I_G peak intensity ratio of polycrystalline graphene on silica illustrating the networking of wrinkles.

regions to deconvolve the effects of different types of nanoscale defects on the modulation of mechanical and electrical properties. Different phonon vibrational characteristics are used to distinguish defects from the DF counterpart. Subsequently, we measured strain and doping distribution (primarily from the underlying substrate) by monitoring the shift in Raman modes in graphene and MoS_2. Controlled AFM-based indentations were carried out which reveal a reduction in the stiffness of the defective regions as compared to the DF regions. Atomic-scale simulations of the distribution of strain along

ripple defects, as an approximation to the experimentally observed defects, were achieved through density functional theory (DFT) and the subsequent effect on electronic properties was studied through band structure calculations. The critical insights presented in this work, combining nanoscale experimental and computational studies, will play an essential role in the future design and fabrication of 2D materials to evaluate and tune their application-specific mechanical and transport properties.

RESULTS AND DISCUSSION

Morphology of Structural Defects. Two-dimensional materials, either from industrially scalable CVD or laboratorybased ME procedures, are inevitably subject to structural defect formation. Here, we focus on different nanoscale line defects and pit-holes comprising out-of-plane deformation and broken lattice symmetry. Figure 1 shows nanoscale imaging through AFM and Raman mapping of structural defects of MEMoS_2, CVD-MoS_2, ME-Gr, and CVD-Gr. The region marked by the dashed rectangle/line in Figure 1a−e shows illustrations of a standing collapsed wrinkle in ME-MoS_2, pit-holes in CVDMoS_2, the transition from wrinkle in ME-Gr, and a nanobubble and a grain boundary in CVD-Gr, respectively. The average thicknesses of ME-MoS_2 and CVD-MoS_2 are measured as 0.93 ± 0.20 and 0.67 ± 0.40 nm, respectively which indicates them to be single layer (see Supporting Figure S1a,b). Nevertheless, the presence of wrinkles and ripples in ME-MoS_2 and adsorbed airborne impurities in CVD-MoS_2 causes wide deviation from the average values. Wrinkles are generated in the 2D sheets due to interfacial compressive strain between the substrate and the physically deposited sheet. The release of compressive strain culminates in a buckled structure due to low bending rigidity of the thin sheet[8] (see Supporting Figure S2 for the AFM micrograph, height profile, and adhesion force map).

The pit-holes in epitaxially grown MoS_2 are formed by etching of the silica substrate due to alkali metal (Na) used during fabrication.[30] The density of the pit-holes varies with concentration of Na^+ precursor and the processing temperature in the CVD chamber. We do not observe the presence of wrinkles in CVD-MoS_2 due to its higher TEC (7.6×10^{-6} K^{-1}) than the underlying silica substrate (0.5×10^{-6} K^{-1}).[31,32] During cooling in the fabrication process, MoS_2 contracts more than silica, leading to tensile strain which prevents wrinkle formation.[9] The bending rigidity of graphene is more than 10 times lower than that of MoS_2,[33] and thus, a higher prevalence of wrinkles has been observed in the former. The trapping of gaseous molecules under the graphene layer in ambient conditions results in the formation of nanobubbles with varying height from 4 to 50 nm during heat treatment.[34] These distorted structures influence strain, doping, and stiffness in their extraordinary way which are investigated through Raman spectroscopy.

Raman Mapping of Structural Defects. The strain and doping contribution made by structural defects in MoS_2 and graphene are studied by Raman spectroscopy in ambient conditions, where the typical Raman modes of MoS_2 and graphene are shown in parts f and g, respectively, of Figure 1.

Raman modes of MoS_2, E^1_{2g}, and A_{1g} are observed at 384 and 403 cm^{-1} and are associated with in-plane and out-of-plane vibration, respectively.[35] Weakened interlayer interaction is observed through the phonon softening of A_{1g} mode in thinner MoS_2 sheets. A long-range Coulomb interlayer interaction is prevalent in thinner layers as observed through E^1_{2g} modes. Therefore, the difference in Raman shift between Pos(E^1_{2g}) and Pos(A_{1g}) is considered a parameter to determine the thickness

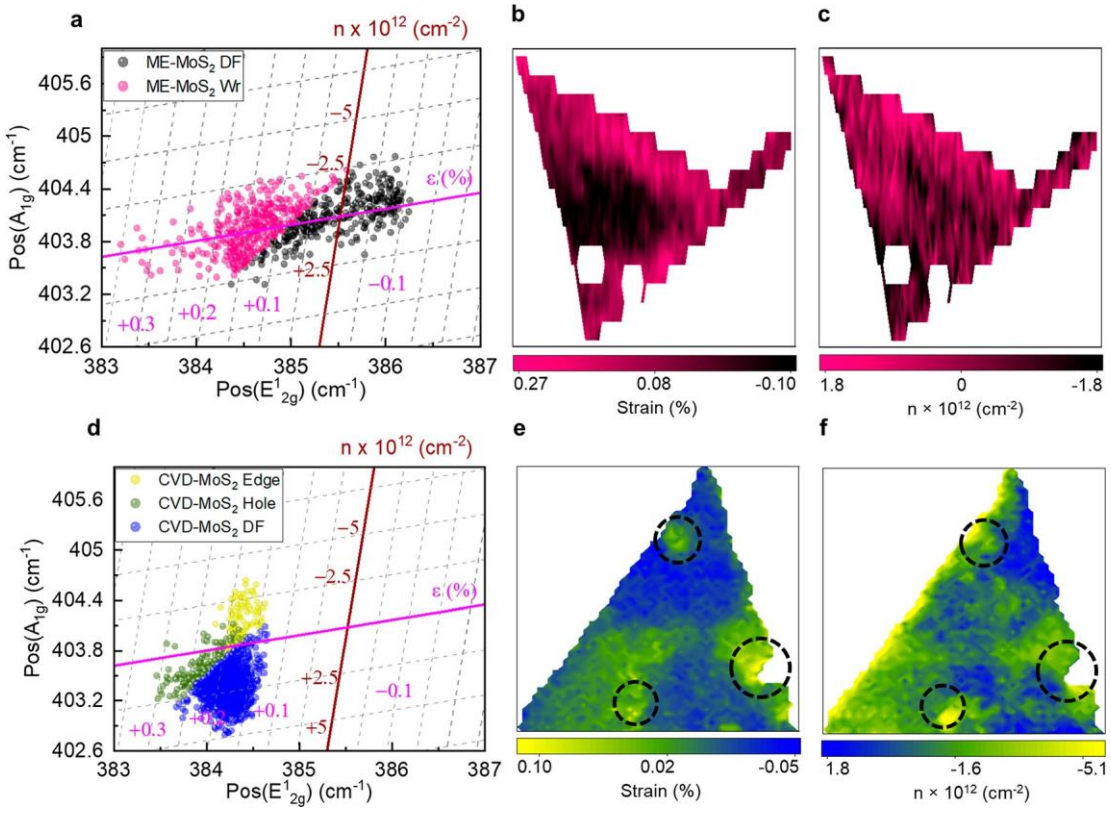

Figure 3. Effect of the structural defects on strain and doping MoS_2. (a) Correlation plot of Pos(E^1_{2g}) versus Pos(A_{1g}) of ME-MoS_2. (b) Strain map of ME-MoS_2 showing the distribution of local strain from flat MoS_2 to the edge region. (c) Doping map of ME-MoS_2 displaying the spatial distribution of charge carrier density (n). (d) Correlation plot for CVD-MoS_2 for CVD/flat, pit-holes, and edge region. (e) Strain and (f) doping maps of epitaxially grown single-layer MoS_2 show edges and pit-holes (marked in circles), induced higher tensile strain, and wide distribution of charge carriers.

of DF MoS_2 flakes. In ME-MoS_2 (Figure 2a,b), we observe the difference in Raman shifts Δ = Pos(A_{1g}) − Pos(E^1_{2g}) to have values of 18, 22, and 23 cm^{-1} for mono-, bi-, and trilayers, respectively.[36] The presence of structural defects alters this trend, which is illustrated by the Raman map of MEMoS$_2$ and CVD-MoS_2 in Figure 2a,b and c,d, respectively. We record phonon softening of the E^1_{2g} mode at wrinkles in MEMoS$_2$ and around pit-holes in CVD-MoS_2 as compared to the surrounding DF region, while a minimal shift is observed for A_{1g} mode. Thus, the presence of wrinkles in monolayer MEMoS$_2$ displays the illusion of a bilayer. Similarly, the Raman modes in CVD-MoS_2 at pit-holes (marked by circles in Figure 2c,d) and edge regions deviate from DF counterparts.

In graphene, D peak intensity (see Supporting Figure S3) and the intensity ratio I_D/I_G serve as indicators for Ramanactive disordered structure and, hence, can be used to monitor the distribution of structural defects such as large wrinkles, edges (zigzag configuration), and damaged/deflated nanobubbles (Figure 2e–j). The D peak does not correspond to a zone center vibrational mode originated from the defects themselves but is attributed to activation of the A_{1g} breathing phonon mode at the K point with momentum q ≠ 0 due to the relaxation of the fundamental Raman selection rule.[18,37] In the pristine crystalline structure of graphene, q ∼ 0 is conserved and the D peak is forbidden. It has been shown that the D peak and its overtone (2D) are susceptible to change in the electronic band structure.[20] The G peak (∼1585 cm^{-1}) corresponds to the E_{2g} phonon mode, which is due to the stretching of sp^2 carbon in graphene. The shifts in Pos(G) and Pos(2D) Raman modes are sensitive to the different geometries of wrinkles and can, therefore, be used to distinguish them. For instance, distinct Raman signals from standing collapsed wrinkles, transitional-folded wrinkles, and folded wrinkles are observed; see Figure 2e,f and Supporting Figure S4 for a Raman map and SEM and AFM micrographs for a complete description. There is a phonon softening of Pos(2D) for the standing collapsed structure and a phonon stiffening for the transitional-folded configuration, but both show redshifts in Pos(G). Similarly, the blueshift in Pos(2D) is also observed for CVD wrinkles (see Supporting Figure S5) as

well as in deflated graphene nanobubble regions (see Supporting Figure S6), indicating the presence of compressive strain as compared to its surrounding DF regions.

Strain and Doping Contribution from Structural Defects. Raman shift measurements are applied to deconvolve strain and doping as described elsewhere;[19,22] see Supporting S7 for a description. Figure 3 illustrates the correlation plot, strain map, and doping map of monolayer ME-MoS_2 and CVD-MoS_2. In the correlation plot, the intersection coordinate of the strain and doping axis is assumed to be minimally strained and doped by the substrate and considered as a reference, which is taken from the average value of our experimental ME-MoS_2 DF data and suspended graphene from elsewhere.[19] The dissimilarity in reference selection approach arises from the different chemical composition between

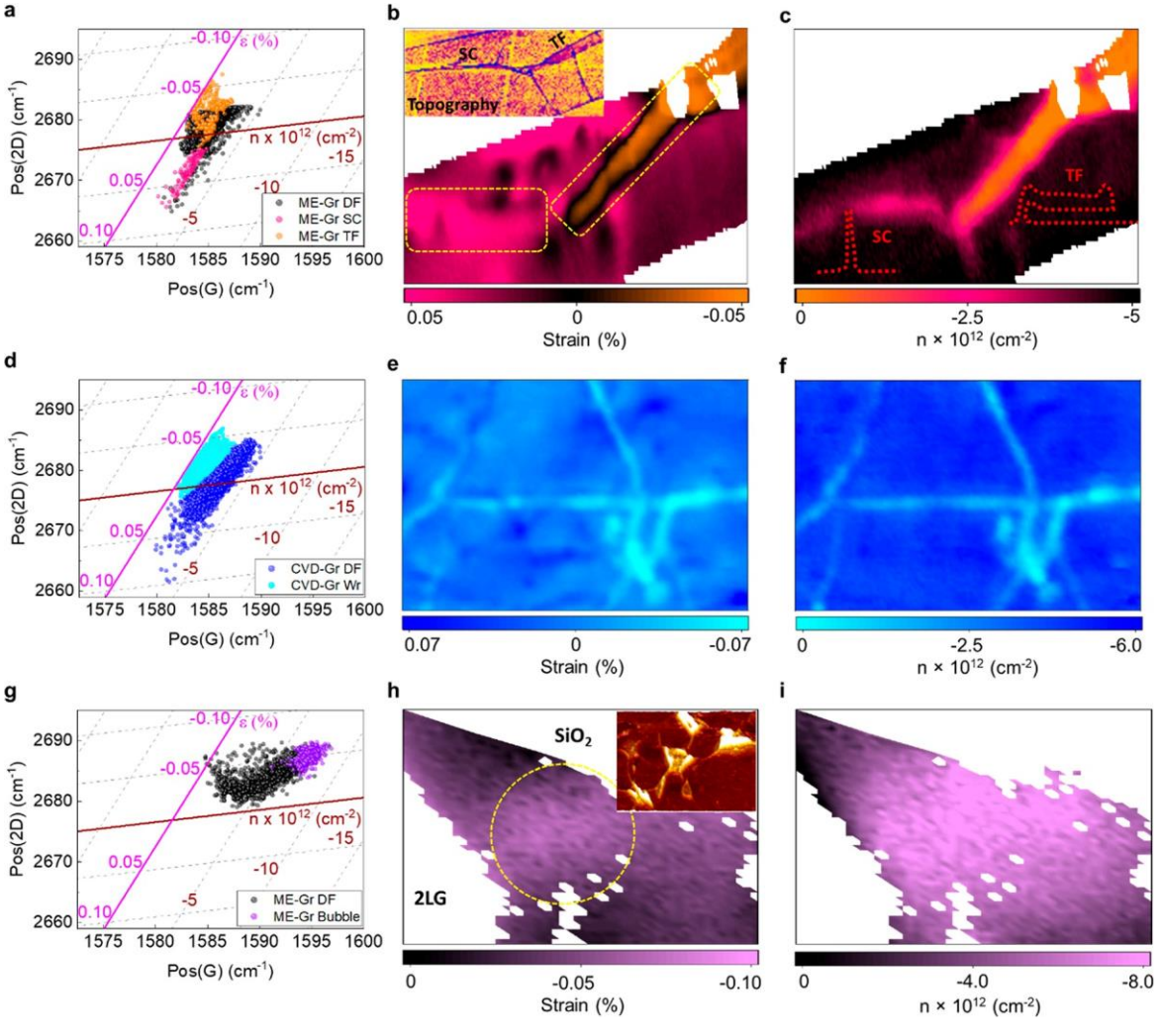

Figure 4. Effects of the structural defects on strain and doping graphene. (a) Correlation plots of Pos(G) versus Pos(2D) for ME-Gr. The spreading of data shown in orange is from DF flat graphene. The data from standing collapsed wrinkled area is shown in black, while orange data distribution represents transitional folding wrinkle. (b) Strain map of ME-Gr derived from Raman data and AFM topography (inset) show tensile and compressive strain from two different geometries of wrinkles. The regions marked with dashed rectangles are standing collapsed and transitional-folded wrinkles. (c) The doping map shows the distribution of charge carriers for two different geometries of wrinkles. Inset: schematic illustration of standing collapsed wrinkle and transitional-folded wrinkle. (d) Correlation plot of CVD-Gr resembles ME-Gr in panel (a). (e) Strain map of the polycrystalline graphene shows compressive strain at wrinkles as compared to the flat region; some wrinkles are also showing tensile strain. (f) The carrier concentration in polycrystalline graphene shows the wide distribution of charge, where the wrinkle has higher n. (g) The correlation plot of the deflated graphene nanobubble shows low electron concentration and higher compressive strain than its surrounding flat graphene. (h) The strain map of the six nanobubbles on ME-Gr shows the distribution of compressive stress in the encircled region; white region is silica substrate and bi-graphene. The inset is an AFM micrograph showing the shape and arrangement of the nanobubble density. (i) The doping map depicts lower n in the nanobubble region as compared to the surrounding flat graphene.

graphene and MoS_2. Graphene only comprises a single layer of carbon atoms, but MoS_2 comprises a S−Mo−S layer, which makes MoS_2 more prone to doping by ambient conditions. Therefore, there are no broadly accepted values for strain- and

doping-free MoS_2, compared to both experimentally and theoretically reproducible values for suspended graphene. The deposition or growing of 2D sheets over silica substrates induces both strain and doping which may be discerned using the correlation plot. Any modified interaction between the 2D sheet and the substrate such as wrinkles, pit-holes, and edges can also be detected. The correlation plot of ME-MoS_2 reveals a wide distribution of strain ε (−0.1 to +0.3%). The DF flat region shows a range of tensile and compressive strain from +0.15 to −0.1% as shown in black in Figure 3a. It indicates variable interfacial coupling between ME-MoS_2 and silica substrates even for the flat sheet. The strain map at Figure 3b is clearly showing the accumulation of the compressive strain at the central flat region (black, ε = −0.09 to −0.01%) which is gradually released at the wrinkled region (dark pink, ε = 0.08− 0.14%) and at the edge region of the MoS_2 sheet (bright pink, ε = 0.14−0.27%). The appearance of the localized strain around the edge and the step-edge region could be related to the edge relaxation mechanism applicable for both armchair and zigzag configuration.[38] It includes the adjustment of bond length and bond angles of the edge atoms to minimize the excess energy generated during mechanical exfoliation.[39] Recently, high-resolution analysis of MoS_2 edges reveals the adjustment of the terminal ends in the formation of concave and convex structure which can tune the strain field from compressive to tensile.[38] In the present investigation, the micron-scale Raman probe is not able to resolve the atomic configuration of the edge sheet, and thus, a high-resolution topographic image concurrent to elastic properties (by force− distance measurement) has been carried out over the relocated region of ME-MoS_2. The atomically resolved edge from AFM illustrates the stretched atoms of S−Mo−S bonds which is revealed by comparing with the unstrained MoS_2 (2×2 nm^2) from DFT study and validated by the AFM line profile. We also observed that the nanoscopic edge region (up to displacement of 250 nm) has an out-of-plane distortion (∼400 pm) as compared to the DF basal plane. There is a relative drop in the stiffness (up to 2−3%) from basal plane to the edge region also (see Supporting Information Figure S8). These findings indicate tensile strain at the edge of ME-MoS_2, which is consistent with the prediction by Tinoco and co-workers.[38]

The wrinkled region in ME-MoS_2 of standing collapsed geometry (see profile from AFM at supplementary Figure S2) shows tensile strain. Local strain influences the carrier distribution in the MoS_2 sheet, and higher electron concentration at the edge region has been observed (Figure 3(c)). It shows the intrinsic tensile strain increases the mobility of the charge carrier. These effects are also observed in other TMDs at small external tensile strain due to incremental changes in the energy gap at the K and Q valleys.[40]

Figure 3d shows MoS_2 epitaxially grown over silica with a tensile strain over the entire sheet in contrast to ME-MoS_2 and higher n, indicating stronger coupling with the substrate than ME-MoS_2. The presence of built-in tensile strain in CVDMoS_2 is attributed to the mismatch in the thermal expansion between MoS_2 and silica substrate from 800 °C to room temperature resulting in tensile strain.[9] At the pit-hole regions, the interaction between MoS_2 and silica is modified relative to the flat region. The pit-hole region can be considered as a circular trench where the MoS_2 sheet is bent around the circular ring that leads to an increase in tensile strain ranging from 0.01% to 0.07%. Unlike ME-MoS_2, the edge region in the CVD-MoS_2 sheet does not induce distinguishable strain (Figure 3e). Nevertheless, it shows a wide range of n in Figure 3f that might be due to different configurations of their terminal atoms (Mo, S/Mo, and S termination). It has been reported that these terminations have a different affinity toward airborne impurities that act as electron transfer site to/ from adsorbed species.[6]

The correlation plot of Raman modes Pos(G, 2D) of graphene and its associated local strain and doping are given in Figure 4. ME-Gr shows a broad range of interactions with the silica substrate as revealed from the wide distribution of strain ε (−0.03 to +0.07%). The irregular conformation of graphene over the substrate is regulated by the adhesion forces between graphene and the substrate which result in the compressive strain as compared to free-standing graphene (intersection point of strain and doping axis). Thus, the appearance of ripples/wrinkles/nanobubbles in graphene is a result of balance between adhesion energy and bending energies. Generally, an excess length (2D material length compared to substrate length) of at least $L_m \sim 24(k/2\beta)^{1/2}$ is required for the transition from a ripple to a folded wrinkle (FW), where k is the bending stiffness and β the binding (vdW) energy per atom thus defining a maximal height for a standing collapsed (SC) wrinkle of $H \sim L_m/2$.[41,42] It has been observed that graphene SC wrinkle sustains its height easily up to 8.4 nm as predicted by $L_m \sim 16.3$ nm ($k = 1.4$ eV, $\beta = 40$ meV); after exceeding the critical height (nearly 8 nm),[43] it starts to bend toward the substrate, albeit not coupled. We refer to this intermediate geometrical state as a transitional-folded wrinkle (TFW). When the wrinkle height is significantly larger than the critical height, the wrinkle finally collapses into a FW, an architecture composed of 3N where N is the number of layers.[42] Therefore, a single-layer graphene results in a strip of trilayer graphene with the modified vertical gap. This geometry alters the electrical and mechanical properties and the interfacial interaction.[44] We deconvoluted the strain and doping in the wrinkled structure up to its TFW state as the parameters used in the correlation plot is limited to a single layer of graphene only verified by monitoring ($I_{2D}/I_G > 1$). The completely folded multilayer graphene revealed by the Raman spectrum $I_{2D}/I_G < 1$ requires distinct parameters; see Supporting Information Figure S4 for different shapes of transformed

wrinkles. The strain map (Figure 4b) and doping map (Figure 4c) for ME-Gr illustrate two distinct geometries of wrinkles, TFW and SC wrinkles, which are also confirmed from AFM topography (inset Figures 4b and S4). The transformation of graphene from SC architecture into TFW geometry results in a transition of Pos(2D) from phonon softening mode to stiffening and, consequently, a transition of strain from tensile to compressive (Supporting Figure S4).

This transformation also influences the doping as follows: TFW ($n \approx -1.1 \times 10^{12}\ cm^{-2}$), SC wrinkle ($n \approx -2.6 \times 10^{12}\ cm^{-2}$), and DF flat region ($n \approx -4.2 \times 10^{12}\ cm^{-2}$). It can be interpreted that prohibition of p-doping occurs when graphene buckles into the SC structure, and this prohibition is strengthened when the wrinkle develops into the TFW architecture. These results are also in good agreement with the high-resolution Kelvin probe force microscopy (KPFM) studies that showed higher electron concentration in the transitional-folded graphene as compared to the standing collapsed wrinkle (see Figure S9). Long et al.[45] have observed through KPFM studies that the vertical gap between graphene and silica substrate can influence the doping in the graphene, which is distinct between SC and FW geometry.

The scatter in the correlation data of CVD-Gr on silica resembles the ME-Gr distribution (see Figure 4d). Nevertheless, the strain and doping maps illustrate higher density of wrinkles/ripples in the CVD system than ME-graphene. It reveals several categories of wrinkles that shows tensile and compressive strain. The region has overcrowding of wrinkles that leads to their merging at the junctions, which enhances the structural disorder as indicated by the I_D/I_G ratio (0.98) and induces compressive strain ε up to (−0.051%) and small magnitude of $n \approx -1.23 \times 10^{12}\ cm^{-2}$ (see Figures 2i,j and 4e,f). The $\Delta n \approx 2.18 \times 10^{12}\ cm^{-2}$ compared to the basal plane being positive implies graphene is less coupled with the substrate and prohibits p-doping. These characteristics are similar to the folded geometry of wrinkles in ME-Gr.

The grain boundary is another line defect in polycrystalline graphene; we performed Raman mapping of a perimeter around a single grain which can provide useful information regarding grain boundaries (see Supporting Figure S10). This region exerts the highest compressive strain as compared to wrinkles and exhibits higher n. The grain boundary comprises local stitches of two grains attached to the substrate, unlike wrinkles which induce a vertical gap; therefore, the grain boundary is influenced by the underlying substrate to induce

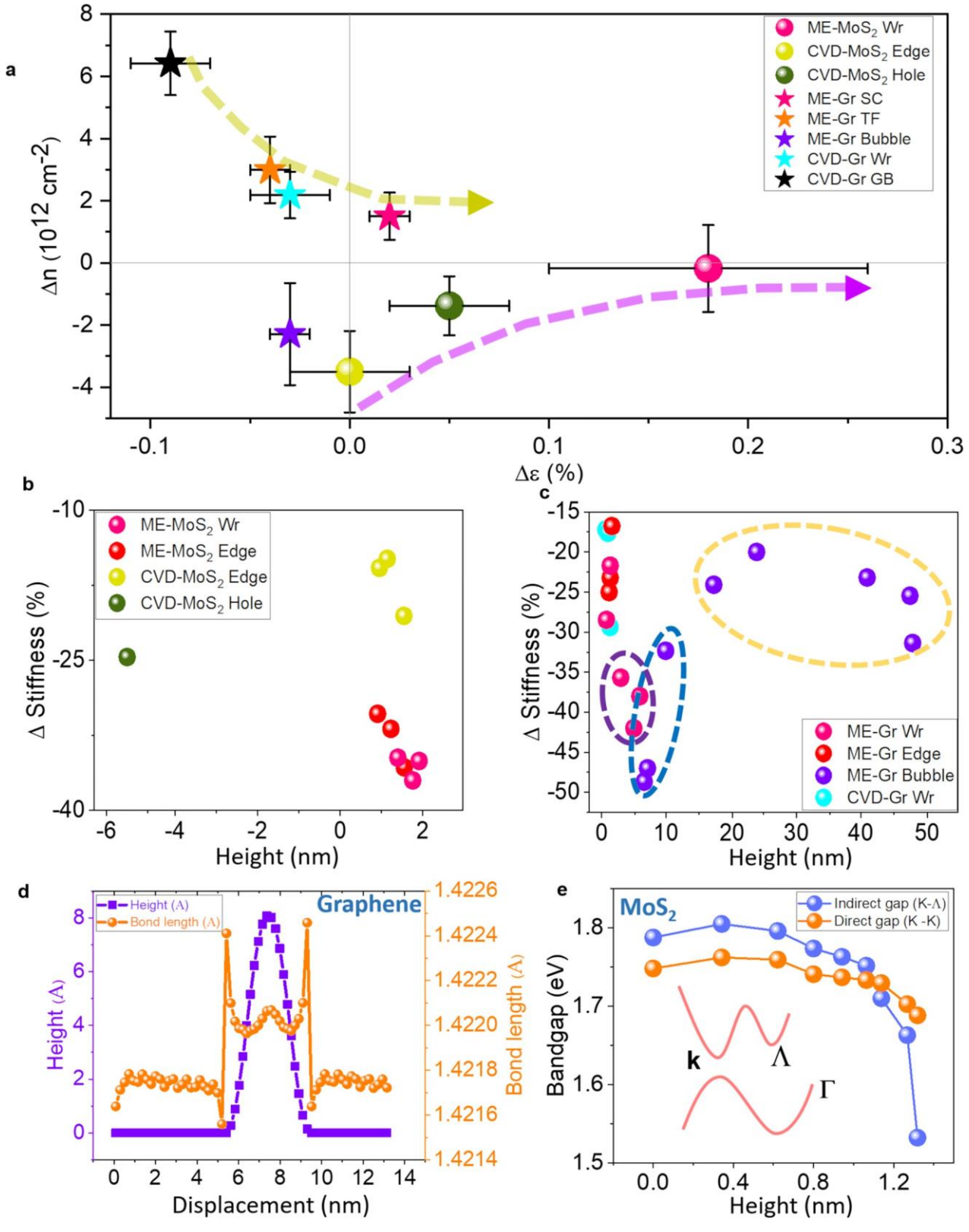

Figure 5. Contribution of the structural defects: (a) Correlation between the relative strain and relative doping from surrounding DF in MoS_2 and graphene. The intersection of solid lines shows the coordinates of zero change in doping and strain. The dashed lines indicate the trend in the change in carrier concentration with increasing tensile strain. Normalized stiffness (%) of different defects of (b) MoS_2 (edge, hole and wrinkle) and (c) graphene (edge, wrinkle, and nanobubble) compared to the flat region. The uncovered data are from standing collapsed wrinkle; data lies in the violet-colored region are from folded wrinkle; the blue shaded region shows a deflated nanobubble and yellow

shaded region shows an inflated nanobubble. (d) DFT calculation of bond length and ripple height across a graphene monolayer defect (e). Bandgap (eV) versus height (nm) of defected MoS_2. The bandgap is modified in MoS_2 due to buckling at the defect and induces a direct-to-indirect transition at higher strain. Inset shows the schematic diagram of the band structure of unstrained MoS_2.

compressive strain. It has been reported through atomistic simulation that the stitching angle between adjacent grains can vary electron concentration and is found to be lowest for θ = 0° and maximum for θ = 30°.[45]

Graphene nanobubbles are inflated formations due to trapped molecules and appear in different shapes such as spherical caps[46] and trigonal[6] and pentagonal geometry (see inset Figure 4h). These structural defects are less prevalent than wrinkles and grain boundaries. We did not find any nanobubble formation in our ME-MoS_2, but six nanobubbles over an occupied surface area of ∼2.25 × 2.8 μm^2 have been observed in ME-Gr. The tensile strain induced by the pressure inside the individual nanobubble is reported up to 0.37% as measured by AFM and Raman spectroscopy.[47] Nevertheless, deflated graphene nanobubbles (see Supporting Figure S11 for topography) behave differently and exert compressive strain (−0.079%) and lower n. It is worth noting that compressive strain is generated from a region of six deflated nanobubbles as marked by a dashed circle in Figure 4h. The present investigation is limited to resolve the contribution from each nanobubble since the diameter of the Raman probe is greater than the defect size (spot size 760 nm and lateral resolution ∼240 nm). Thus, the measured compressive strain and n (Figure 4i) are the accumulation of six nanobubbles. The AFM profile has been used to measure the strain (ε_{AFM}) for the deflated nanobubble. It is found that few partially deflated individual nanobubbles exert tensile strain (ε_{AFM}) up to 0.08% as compared to DF. Still, some nanobubbles induce significant compressive strain (ε_{AFM} = −0.37%) as compared to inflated nanobubbles due to reduction in the perimeter for the latter.

By virtue of the correlation plot, strain map, and doping map in Figures 3 and 4, we have demonstrated the deconvolution of the absolute strain and doping of each structural defect with respect to the no-strain, no-doping coordinate. Nevertheless, it is also crucial to compare the interaction of each defect with respect to its nearby defect-free surrounding region (relative strain and doping) to provide additional information regarding the direct influence by the defect. This comparison can be drawn at Figure 5a and in the Supporting Information at Table S1 where we subtract the absolute strain and doping of the DF from that of the defect. While defects in MoS_2 are predominantly under tensile strain and all reduce carrier density, this reduction in electron concentration is compensated by increasing strain. Conversely, defects in graphene in general increase the carrier concentration compared to the surrounding DF region, but this surge diminishes with increasing strain. It indicates that for both graphene and MoS_2 the change in carrier concentration (Δn) is reduced with increasing tensile strain. The overall trend also indicates that edges are prone to doping than strain, while wrinkles in 2D materials contribute heavily to strain. The graphene nanobubble behave exceptionally in electronic modulation, and thus, introducing nanobubbles in scalable graphene sheets (i.e., CVD-Gr) may be promising defects to engineer for straintronics.

Mechanical Stiffness of the Structural Defects. The inplane stiffness is lower at the structural defects as compared to the surrounding DF regions owing to out-of-plain distortion in the lattice (see Supporting Figure S12 for details). We observed a higher indentation depth at the structural defects as compared to the DF, which indicates a drop in stiffness. It is suggested that indentation depth required to puncture a suspended sheet is around 50 nm for MoS_2 and ∼150 nm for graphene.[48] We limit our imposed displacement (δ≈ 5 nm) so to have elastic deformation for both tip apex and the sample. The normalized drop-in stiffness (%) of structural defects for MoS_2 is shown in Figure 5b and for graphene in Figure 5c. In MoS_2, the lowest values of elastic stiffness (i.e., 40% reduction) are measured from the wrinkle of height up to 2.9 nm, while the graphene wrinkle is relatively stiffer by a factor of 2.3 at a similar height. This is due to the higher axial bending stiffness of graphene (350 ± 50 N/m) than MoS_2 (180 ± 60 N/m), owing to strong covalent carbon−carbon bonds as compared to the polar covalent S−Mo bond, respectively.[48] It is reported that out-of-plane deformation brings down the stiffness dramatically in a nonlinear fashion in relation to strain and amplitude of the buckled structure.[49] Generally, the bending rigidity of 2D material is defined through the compliance of inplane stiffness and the energy-related out-of-plane formation. In particular, for graphene as a thin atomic layer, the system becomes highly anharmonic during out-of-plane deformation under the influence in-plane stress.[14] For other 2D materials, the out-of-plane deformation (such as ripple and wrinkle) can be explained through its bending rigidity. Nevertheless, it is the scale of deformation (l_{anh}) that can decide the contribution from in-plane stiffness and bending rigidity to the elastic energy of the 2D material. It is expected that the ability to achieve in-plane stress from bending rigidity in graphene is higher than MoS_2 due to difference in the anharmonic scale of deformation (defined as square root of the ratio of the Young's modulus over the bending rigidity) of graphene (0.4 nm) and MoS_2 (between 0.4 and 1 nm). Therefore, the capability to transfer stress in graphene could be higher than MoS_2 of similar geometry.[14]

The stiffness of the inflated graphene nanobubble (20−50 nm height, marked by yellow color) drops up to 17%−30% from its surrounded DF region (see Figure 5c). After deflation (blue), the stiffness further drops to 50% due to the release of internal pressure from trapped gases. The release of trapped gases causes the distorted lattice to behave differently from the wrinkles for strain and doping as confirmed by Raman spectroscopy. The aspect ratio (height over in-plane diameter, h/d) can explain

the interplay between van der Waals and elastic energies of nanobubble-shaped graphene. The reduced (increased) aspect ratio induces tensile (compressive) strain; see Supporting Information Figure S12b. The drop in the stiffness for various aspect ratios, where the aspect ratio of stiffer shapes has been measured around 6×10^{-2}, suggesting that trigonal- and pentagonal-shaped graphene nanobubbles are stiffer.

First-principles DFT is implemented using the ripple structure in graphene and MoS_2 as an approximation to the larger amplitude experimentally observed wrinkles and nanobubbles. The interaction of flat MoS_2 and the graphene monolayer with the silica substrate (as α-quartz SiO_2) is investigated in different configurations as fully reconstructed and partially exposed dangling bonds through hydrogen passivation; see Supporting Figure S13 for details. The choice of α-quartz SiO_2 is due to its stable crystalline phase at ambient conditions. We observed p-doping in adsorbed graphene and MoS_2 monolayer over dangling oxygen bonds at the SiO_2 interface. Additionally, periodic supercells of graphene and MoS_2 are constructed as in Figure S14a,b, wherein the unit cell is repeated a number of times in the armchair direction. A net compression is applied to the cell, which is divided into two regions, labeled as I and II for DF and rippled regions, respectively. In region I, the atoms are constrained to remain flat, such that the out-of-plane force component is set to zero during relaxation, while in region II, all atoms are allowed to fully relax. Upon structural relaxation, the resulting strain is accommodated through the out-of-plane buckling in the delaminated region; see Supporting Figure S14c,d for strain− height and curvature−strain correlations. The strain accommodation across the defected cell was then analyzed by extracting the variation in bond length with increasing ripple height, while electronic properties have been examined through band structure calculations. Our simulations indicate that the net bond compression depends upon the orientation of individual bonds with respect to the applied strain (further details regarding this and boundary conditions across the flat regions are provided in Supporting Information Figure S15).

The exceptional rigidity of monolayer graphene seen in our experiments is also evident in the theoretical calculations. For both materials, the bond strain across a defect is generally tensile (for more details, see Supporting Figure S16), while the change in bond length across graphene ripples does not exceed 0.3% for any height, as in Figure 5d. In contrast, deformed MoS_2 shows more exaggerated distortion of the bonds over a buckled region, with a larger variation in the Mo−Mo (∼0.8%) and Mo−S (∼2−3%) bond lengths at equivalent equilibrium heights, a fact which we attribute to the stronger covalent C−C bond of graphene. The bond lengths in the vicinity of a buckled region of MoS_2 demonstrate both the larger distortion of the Mo−S bond length and the asymmetry in this distortion, which is alternately compressive or tensile dependent on the relative orientation of the Mo and S atoms; see Supporting Figure S14b.

Band structure calculations of defective MoS_2 show that the inhomogeneous variation in bond length across a ripple also has a pronounced effect on its electronic properties due to the change in the length and angle of the Mo−S bonds, as shown in Figure 5e. At small equilibrium ripple heights, corresponding to less applied strain, buckling results in a moderate increase in the direct bandgap of a MoS_2 layer, while at larger heights (>1 nm) there is a systematic drop in the band gap and a transition from a direct to an indirect gap semiconductor (see the systematic band gap transition in Figure S17). The transition of the Λ valley in the conduction band to a lower energy than the K valley is responsible for this conversion of direct to indirect band gap.[50] This effect is also observed in the photoluminescence which decreases dramatically under tensile strain. This transition has been observed for both compressive and tensile strain in the monolayer of MoS_2. As in the case of ripple (for tensile strain), there is a transition of the valence band maximum from (K) to (Γ) valley.[50]

CONCLUSION

Here, we have addressed the contribution of structural defects generated during fabrication and transfer of 2D materials over silica substrates to the electronic and nanomechanical properties of the materials themselves. By monitoring the morphology and Raman modes of graphene and MoS_2, we observed that the geometry of structural defects plays an essential role in the strain, doping and mechanical stiffness in the studied 2D materials. The physical deposition of graphene and MoS_2 have compressive strain from the silica substrates at the defect-free regions, which is effectively released at wrinkles with a standing-collapsed geometry. Nevertheless, the other geometrical architectures of folded wrinkles, grain boundaries or deflated nanobubbles exert higher compressive strain as compared to surrounding DF graphene. The substrate also acts as a dopant to the 2D sheets, which varies at the defect center. Unlike ME procedure, CVD-MoS_2/silica induces tensile strain in the TMD sheet, the edges of the MoS_2 sheet have a broad range of n depending on the terminal ends of edge atoms and adsorption of airborne impurities. The stiffness of out-of-plane architecture of 2D layers steeply decreases with the amplitude of the buckled structure until the internal pressure regulates the resistance against mechanical deformation as in the case of inflated graphene nanobubbles. The graphene wrinkles are found to be stiffer than MoS_2 of similar geometry due to accumulation of higher strain accommodation in the MoS_2 as revealed by DFT calculations. Associated to these structural changes, we see modulation of the size of the band gap due to the defect and a transition from direct to indirect gap at higher strains in MoS_2. This approach allows us to make important intuitive observations about structural defects such as wrinkles exhibiting significant strain but minimal doping and edges exhibiting minimal strain but significant doping. In addition, defects

in graphene predominantly show compressive strain and increased carrier density while defects in MoS_2 predominantly show tensile strain and reduced carrier density. Furthermore, increasing tensile strain is found to decrease doping across all defects in both materials. The presented work unravels path for device performance based on straintronics and defect engineering.

MATERIALS AND METHODS

Sample Fabrication. ME-MoS_2 graphene is transferred to a silica substrate with 300 nm thickness of oxide. It is then cleaned in ultrasonic bath for 30 min in 2-propanol and subsequently deionized water, and then heated in vacuum oven 200 °C for 3 h to remove organic impurities. CVD graphene is commercially obtained from Graphenea (Graphenea, Inc., Spain). CVD-MoS_2 crystals were grown by employing the fabrication method reported in the literature.[51] In brief, Si wafers with a 90 nm thick SiO_2 layer were spin coated with an aqueous solution of 2 mg/mL $NaMoO_4$. Subsequently the wafers were placed in a two-zone high temperature furnace. The main zone (containing the substrates) was heated to a growth temperature of 750 °C with a rate of 10 °C/min. When the main zone reached the growth temperature, the second zone located upstream and containing a quartz crucible loaded with 2 g of S was heated to 230 °C. Both zones were kept at these temperatures for 15 min, and afterward, the tube was removed from the furnace and allowed to cool to room temperature. It is worth noting that selection of temperature is pivotal to control the "pit-holes" structural defect; even reduction of temperature by 50−100 °C can alter the density of pit-holes. Raman Spectroscopy. Raman spectroscopy is performed by Renishaw inVia confocal Raman microscope with 532 nm laser (type: solid state, model RL53250) and 1800 mm^{-1} grating in 100× magnification. Details about peak position accuracy is given in the Supporting Information in Figure S18. The Raman spectra for graphene samples were measured at 1.5 mW of power, while those of MoS_2 samples were measured at 0.15 mW of power for a duration of 1 s. The output power of the laser is separately monitored by a power meter (model: Gentec, PH 100-Si-HA-D0). The effect of the laser is separately studied over DF ME-MoS_2 and ME-Gr, and no overheating effect has been observed in terms of shifting of Raman peak positions. The peak intensity and peak position are determined by Lorentz curve fitting.

AFM Characterization. AFM characterization is carried out by Bruker Dimension Icon with PF-QNM (PeakForce-Quantitative NanoMechanical) mode, where topology, adhesion, and stiffness are measured on a single acquisition. Cantilevers are calibrated by preceding thermal tune for resonance frequency and stiffness, which are measured as 535 kHz and 200 ± 10 N/m, respectively, for stiffness measurement as well as 0.4 N/m and 70 kHz for topology and adhesion measurement. Kelvin Probe force microscopy (KPFM) was carried out by AFM-Bruker Dimension Icon at ambient condition over antivibrant stage. Contact potential difference (CPD, mV) was measured from advanced operation mode of Peak-force KPFM using a two-pass technique mode. In the first pas, the tip was softly (<1 nN) tapped on top of the sample to gather topographical data. In the second pass, the same scanning line, the cantilever was lifted from the surface up to 10 nm distance to collect CPD data. Silicon−nitride probe model: PFQNE-AL, tip diameter around 5 nm, and stiffness 0.8 ± 0.2 N/m was used for the investigation. Thermal tune calibration was performed before to monitor the stiffness of the cantilever. Freshly cleaved graphite (HOPG, WF = 4.66 eV) was used to measure the WF of tip: WF (sample) = WF(tip) − eV(dc). The same relation is also used to measure the WF of the sample.

Scanning Electron Microscopy. SEM is operated by Zeiss SIGMA field emission gun with working distance of 2 mm and an accelerating voltage of 1 kV.

DFT. First-principles DFT simulations have been performed using the Quantum Espresso package.[52,53] Vanderbilt ultrasoft Perdew−Burke−Ernzerhof (PBE) pseudopotentials are used to model all atomic species,[54,55] and an energy cutoff of E_{cut} = 40 Ry is found to achieve high convergence. A 5 × 5 × 1 k-point grid has been used for calculations of monolayer-SiO_2 adsorption, while a 5 × 1 × 1 k-point sampling is applied to the rippled supercells, each giving an overall convergence to within 0.1 meV/atom of the more highly converged calculations. The van der Waals interaction is modeled using the optB86b-vdW functional, as implemented in Quantum Espresso. All Brillouin-zone integrations are performed on a Γ-centered mesh generated according to the Monkhorst−Pack method and a Gaussian smearing of width 0.01 eV is applied. Structures are optimized until the force on all atoms is less than 1 × 10^{-3} eV/Å, and the energy change is less than 1 × 10^{-4} eV. Electronic band structures are calculated using a more highly converged 15 × 2 × 1 k-point grid.

ASSOCIATED CONTENT

* Supporting Information

The Supporting Information is available free of charge at https://pubs.acs.org/doi/10.1021/acsnano.0c06701.

Thickness measurements of graphene and MoS_2 (S1). Adhesion force map of the structural defects in concurrent with topography (S2). Raman spectra and mapping of ME and CVD graphene (S3−S6).

Correlation plot measurement using Grüneisen parameters and strain rate of MoS_2 and graphene to generate strain and doping map (S7). Physical and elastic properties of the MoS_2 edge (S8). Surface potential map of wrinkle in ME-Gr (S9). Raman mapping of grain boundary in CVD-graphene showing strain, doping, and ID/IG ratio (S10). AFM image of inflated and deflated individual nanobubble (S11). Force−distance spectra and stiffness map of graphene and MoS_2 (S12). DFT calculations showing electronic band structure, heightstrain relation and accumulation of strain at the rippled structure (S13−17). Determination of spectral accuracy using Si wafer as reference (S18)(PDF)

AUTHOR INFORMATION

Corresponding Authors

Manoj Tripathi − Department of Physics and Astronomy, University of Sussex, Brighton BN1 9RH, United Kingdom; orcid.org/0000-0002-8052-428X; Email: m.tripathi@sussex.ac.uk

Alan B. Dalton − Department of Physics and Astronomy, University of Sussex, Brighton BN1 9RH, United Kingdom; orcid.org/0000-0001-8043-1377; Email: a.b.dalton@sussex.ac.uk

Pulickel M. Ajayan − Department of Materials Science and NanoEngineering, Rice University, Houston, Texas 77005, United States; Email: pma2@rice.edu

Authors

Frank Lee − Department of Physics and Astronomy, University of Sussex, Brighton BN1 9RH, United Kingdom

Antonios Michail − Department of Physics, University of Patras, Patras GR26504, Greece; Institute of Chemical Engineering Sciences, Foundation for Research and Technology- Hellas (FORTH/ICE-HT), Patras GR26504, Greece

Dimitris Anestopoulos − Institute of Chemical Engineering Sciences, Foundation for Research and Technology- Hellas (FORTH/ICE-HT), Patras GR26504, Greece

James G. McHugh − Department of Chemistry, Loughborough University, Loughborough LE11 3TU, United Kingdom

Sean P. Ogilvie − Department of Physics and Astronomy, University of Sussex, Brighton BN1 9RH, United Kingdom; orcid.org/0000-0002-0433-8186

Matthew J. Large − Department of Physics and Astronomy, University of Sussex, Brighton BN1 9RH, United Kingdom

Aline Amorim Graf − Department of Physics and Astronomy, University of Sussex, Brighton BN1 9RH, United Kingdom; orcid.org/0000-0003-3071-2255

Peter J. Lynch − Department of Physics and Astronomy, University of Sussex, Brighton BN1 9RH, United Kingdom

John Parthenios − Institute of Chemical Engineering Sciences, Foundation for Research and Technology- Hellas (FORTH/ICE-HT), Patras GR26504, Greece; orcid.org/0000-0001-6066-7120

Konstantinos Papagelis − Institute of Chemical Engineering Sciences, Foundation for Research and Technology- Hellas (FORTH/ICE-HT), Patras GR26504, Greece; School of Physics, Department of Solid State Physics, Aristotle University of Thessaloniki, Thessaloniki 54124, Greece; orcid.org/0000-0001-5094-9837

Soumyabrata Roy − Department of Materials Science and NanoEngineering, Rice University, Houston, Texas 77005, United States

M. A. S. R. Saadi − Department of Materials Science and NanoEngineering, Rice University, Houston, Texas 77005, United States

Muhammad M. Rahman − Department of Materials Science and NanoEngineering, Rice University, Houston, Texas 77005, United States

Nicola Maria Pugno − Laboratory of Bio-inspired, Bionic, Nano, Meta Materials & Mechanics, University of Trento, I38123 Trento, Italy; School of Engineering and Materials Science, Queen Mary University of London, London E1 4NS,

United Kingdom; orcid.org/0000-0003-2136-2396
Alice A. K. King − Department of Physics and Astronomy,
University of Sussex, Brighton BN1 9RH, United Kingdom; orcid.org/0000-0002-1637-757X
Complete contact information is available at: https://pubs.acs.org/10.1021/acsnano.0c06701

Author Contributions
‡
M.T. and F.L. contributed equally,
Notes
The authors declare no competing financial interest.

ACKNOWLEDGMENTS

We acknowledge strategic development funding from the University of Sussex. PMA acknowledges support from the Air Force Office of Scientific Research under award number FA9550-18-1-0072. JGM acknowledges the use of the HPCMidlands+ facility, funded by EPSRC grant EP/ P020232/1 as part of the HPC Midlands+ consortium.

REFERENCES

(1) Wang, Y.; Shi, Z.; Huang, Y.; Ma, Y.; Wang, C.; Chen, M.; Chen, Y. Supercapacitor Devices Based on Graphene Materials. J. Phys. Chem. C 2009, 113 (30), 13103−13107.
(2) Bonaccorso, F.; Sun, Z.; Hasan, T.; Ferrari, A. C. Graphene Photonics and Optoelectronics. Nat. Photonics 2010, 4 (9), 611−622.
(3) Ben Amara, I.; Ben Salem, E.; Jaziri, S. Optoelectronic Response and Excitonic Properties of Monolayer MoS2. J. Appl. Phys. 2016, 120 (5), 051707.
(4) Jiang, T.; Liu, H.; Huang, D.; Zhang, S.; Li, Y.; Gong, X.; Shen, Y.-R.; Liu, W.-T.; Wu, S. Valley and Band Structure Engineering of Folded MoS2 Bilayers. Nat. Nanotechnol. 2014, 9 (10), 825.
(5) Qi, Z.; Cao, P.; Park, H. S. Density Functional Theory Calculation of Edge Stresses in Monolayer MoS2. J. Appl. Phys. 2013, 114 (16), 163508.
(6) Zhang, X.; Xin, J.; Ding, F. The Edges of Graphene. Nanoscale 2013, 5 (7), 2556−2569.
(7) Tsen, A. W.; Brown, L.; Levendorf, M. P.; Ghahari, F.; Huang, P. Y.; Havener, R. W.; Ruiz-Vargas, C. S.; Muller, D. A.; Kim, P.; Park, J. Tailoring Electrical Transport across Grain Boundaries in Polycrystalline Graphene. Science 2012, 336 (6085), 1143−1146.
(8) Chen, W.; Gui, X.; Yang, L.; Zhu, H.; Tang, Z. Wrinkling of Two-Dimensional Materials: Methods, Properties and Applications. Nanoscale Horizons 2019, 4 (2), 291−320.
(9) Liu, Z.; Amani, M.; Najmaei, S.; Xu, Q.; Zou, X. L.; Zhou, W.;
Yu, T.; Qiu, C. Y.; Birdwell, A. G.; Crowne, F. J.; Vajtai, R.; Yakobson, B. I.; Xia, Z. H.; Dubey, M.; Ajayan, P. M.; Lou, J. Strain and Structure Heterogeneity in MoS2 Atomic Layers Grown by Chemical Vapour Deposition. Nat. Commun. 2014, 5, 1−9, DOI: 10.1038/ ncomms6246.
(10) Qin, Z.; Taylor, M.; Hwang, M.; Bertoldi, K.; Buehler, M. J. Effect of Wrinkles on the Surface Area of Graphene: toward the Design of Nanoelectronics. Nano Lett. 2014, 14 (11), 6520−6525.
(11) Si, C.; Sun, Z.; Liu, F. Strain Engineering of Graphene: A Review. Nanoscale 2016, 8 (6), 3207−3217.
(12) Scalise, E.; Houssa, M.; Pourtois, G.; Afanas'ev, V.; Stesmans, A. Strain-Induced Semiconductor to Metal Transition in the TwoDimensional Honeycomb Structure of MoS2. Nano Res. 2012, 5 (1), 43−48.
(13) Mueller, N. S.; Heeg, S.; Alvarez, M. P.; Kusch, P.; Wasserroth, S.; Clark, N.; Schedin, F.; Parthenios, J.; Papagelis, K.; Galiotis, C. Evaluating Arbitrary Strain Configurations and Doping in Graphene with Raman Spectroscopy. 2D Mater. 2018, 5 (1), 015016.
(14) Khestanova, E.; Guinea, F.; Fumagalli, L.; Geim, A. K.; Grigorieva, I. V. Universal Shape and Pressure inside Bubbles Appearing in van der Waals Heterostructures. Nat. Commun. 2016, 7, 12587.
(15) Yue, K.; Gao, W.; Huang, R.; Liechti, K. M. Analytical Methods for the Mechanics of Graphene Bubbles. J. Appl. Phys. 2012, 112 (8), 083512.
(16) Androulidakis, C.; Koukaras, E. N.; Carbone, M. G. P.; Hadjinicolaou, M.; Galiotis, C. Wrinkling Formation in SimplySupported Graphenes under Tension and Compression Loadings. Nanoscale 2017, 9 (46), 18180−18188.
(17) Nirmalraj, P. N.; Thodkar, K.; Guerin, S.; Calame, M.; Thompson, D. Graphene Wrinkle Effects on Molecular Resonance States. npj 2D Materials and Applications 2018, 2 (1), 8.
(18) Si, C.; Liu, Z.; Duan, W.; Liu, F. First-Principles Calculations on the Effect of Doping and Biaxial Tensile Strain on ElectronPhonon Coupling in Graphene. Phys. Rev. Lett. 2013, 111 (19), 196802.
(19) Lee, J. E.; Ahn, G.; Shim, J.; Lee, Y. S.; Ryu, S. Optical Separation of Mechanical Strain from Charge Doping in Graphene. Nat. Commun. 2012, DOI: 10.1038/ncomms2022.
(20) Ferralis, N. Probing Mechanical Properties of Graphene with Raman Spectroscopy. J. Mater. Sci. 2010, 45 (19), 5135−5149.
(21) Lazzeri, M.; Mauri, F. Nonadiabatic Kohn Anomaly in a Doped Graphene Monolayer. Phys. Rev. Lett. 2006, 97 (26), 266407.
(22) Michail, A.; Delikoukos, N.; Parthenios, J.; Galiotis, C.; Papagelis, K. Optical Detection of Strain and Doping Inhomogeneities in Single Layer MoS2. Appl. Phys. Lett. 2016, 108 (17), 173102.

(23) Pimenta, M. A.; del Corro, E.; Carvalho, B. R.; Fantini, C.; Malard, L. M. Comparative Study of Raman Spectroscopy in Graphene and MoS2-Type Transition Metal Dichalcogenides. Acc. Chem. Res. 2015, 48 (1), 41−47.
(24) Chen, C.-C.; Bao, W.; Theiss, J.; Dames, C.; Lau, C. N.; Cronin, S. B. Raman Spectroscopy of Ripple Formation in Suspended Graphene. Nano Lett. 2009, 9 (12), 4172−4176.
(25) Castellanos-Gomez, A.; Roldan, R.; Cappelluti, E.; Buscema, M.; Guinea, F.; van der Zant, H. S. J.; Steele, G. A. Local Strain Engineering in Atomically Thin MoS2. Nano Lett. 2013, 13 (11), 5361−5366.
(26) Zhang, Y.; Heiranian, M.; Janicek, B.; Budrikis, Z.; Zapperi, S.; Huang, P. Y.; Johnson, H. T.; Aluru, N. R.; Lyding, J. W.; Mason, N. Strain Modulation of Graphene by Nanoscale Substrate Curvatures: A Molecular View. Nano Lett. 2018, 18 (3), 2098−2104.
(27) Rao, R.; Islam, A. E.; Singh, S.; Berry, R.; Kawakami, R. K.; Maruyama, B.; Katoch, J. Spectroscopic Evaluation of ChargeTransfer Doping and Strain in Graphene/MoS2 Heterostructures. Phys. Rev. B: Condens. Matter Mater. Phys. 2019, DOI: 10.1103/PhysRevB.99.195401.
(28) Lee, T.; Mas'ud, F. A.; Kim, M. J.; Rho, H. Spatially Resolved Raman Spectroscopy of Defects, Strains, and Strain Fluctuations in Domain Structures of Monolayer Graphene. Sci. Rep. 2017, 7 (1), 16681.
(29) Nicholl, R. J. T.; Conley, H. J.; Lavrik, N. V.; Vlassiouk, I.; Puzyrev, Y. S.; Sreenivas, V. P.; Pantelides, S. T.; Bolotin, K. I. The Effect of Intrinsic Crumpling on the Mechanics of Free-Standing Graphene. Nat. Commun. 2015, 6, 8789.
(30) Choi, S. H.; Kim, Y. J.; Yang, W.; Kim, K. K. Alkali MetalAssisted Growth of Single-Layer Molybdenum Disulfide. J. Korean Phys. Soc. 2019, 74 (11), 1032−1038.
(31) Zhang, L.; Lu, Z.; Song, Y.; Zhao, L.; Bhatia, B.; Bagnall, K. R.; Wang, E. N. Thermal Expansion Coefficient of Monolayer Molybdenum Disulfide Using Micro-Raman Spectroscopy. Nano Lett. 2019, 19 (7), 4745−4751.
(32) Tada, H.; Kumpel, A. E.; Lathrop, R. E.; Slanina, J. B.; Nieva, P.; Zavracky, P.; Miaoulis, I. N.; Wong, P. Y. Thermal Expansion Coefficient of Polycrystalline Silicon and Silicon Dioxide Thin Films at High Temperatures. J. Appl. Phys. 2000, 87 (9), 4189−4193.
(33) Gonzalez, R. I.; Valencia, F. J.; Rogan, J.; Valdivia, J. A.; Sofo, J.́; Kiwi, M.; Munoz, F. Bending Energy of 2D Materials: Graphene, MoS2 and Imogolite. RSC Adv. 2018, 8 (9), 4577−4583.
(34) Jain, S. K.; Juricic, V.; Barkema, G. T. Probing the Shape of a Graphene Nanobubble. Phys. Chem. Chem. Phys. 2017, 19 (11), 7465−7470.
(35) Lee, C.; Yan, H.; Brus, L. E.; Heinz, T. F.; Hone, J.; Ryu, S. Anomalous Lattice Vibrations of Single- and Few-Layer MoS2. ACS Nano 2010, 4 (5), 2695−2700.
(36) Li, H.; Zhang, Q.; Yap, C. C. R.; Tay, B. K.; Edwin, T. H. T.; Olivier, A.; Baillargeat, D. From Bulk to Monolayer MoS2: Evolution of Raman Scattering. Adv. Funct. Mater. 2012, 22 (7), 1385−1390.
(37) Tuinstra, F.; Koenig, J. L. Raman Spectrum of Graphite. J. Chem. Phys. 1970, 53 (3), 1126−1130.
(38) Tinoco, M.; Maduro, L.; Masaki, M.; Okunishi, E.; Conesa-Boj, S. Strain-Dependent Edge Structures in MoS2 Layers. Nano Lett. 2017, 17 (11), 7021−7026.
(39) Huang, Y.; Ling, C.; Liu, H.; Wang, S. Edge-, Width- and Strain-Dependent Semiconductor−Metal Transition in SnSe Nanoribbons. RSC Adv. 2014, 4 (14), 6933−6938.
(40) Hosseini, M.; Elahi, M.; Pourfath, M.; Esseni, D. Strain-Induced Modulation of Electron Mobility in Single-Layer Transition Metal Dichalcogenides. IEEE Trans. Electron Devices 2015, 62 (10), 3192− 3198.
(41) Zhang, J.; Xiao, J.; Meng, X.; Monroe, C.; Huang, Y.; Zuo, J.-M. Free Folding of Suspended Graphene Sheets by Random Mechanical Stimulation. Phys. Rev. Lett. 2010, 104 (16), 166805.
(42) Zhang, K.; Arroyo, M. Adhesion and Friction Control Localized Folding in Supported Graphene. J. Appl. Phys. 2013, 113 (19), 193501.
(43) Zhu, W.; Low, T.; Perebeinos, V.; Bol, A. A.; Zhu, Y.; Yan, H.; Tersoff, J.; Avouris, P.; S. tructure and Electronic Transport in Graphene Wrinkles. Nano Lett. 2012, 12 (7), 3431−3436.
(44) Verhagen, T.; Pacakova, B.; Bousa, M.; Hübner, U.; Kalbac, M.; Vejpravova, J.; Frank, O. Superlattice in Collapsed Graphene Wrinkles. Sci. Rep. 2019, 9 (1), 1−7.
(45) Long, F.; Yasaei, P.; Sanoj, R.; Yao, W.; Kral, P.; Salehi-Khojin,́ A.; Shahbazian-Yassar, R. Characteristic Work Function Variations of Graphene Line Defects. ACS Appl. Mater. Interfaces 2016, 8 (28), 18360−18366.
(46) Zabel, J.; Nair, R. R.; Ott, A.; Georgiou, T.; Geim, A. K.; Novoselov, K. S.; Casiraghi, C. Raman Spectroscopy of Graphene and Bilayer under Biaxial Strain: Bubbles and Balloons. Nano Lett. 2012, 12 (2), 617−621.
(47) Huang, Y.; Wang, X.; Zhang, X.; Chen, X.; Li, B.; Wang, B.; Huang, M.; Zhu, C.; Zhang, X.; Bacsa, W. S. Raman Spectral Band Oscillations in Large Graphene Bubbles. Phys. Rev. Lett. 2018, 120 (18), 186104.
(48) Bertolazzi, S.; Brivio, J.; Kis, A. Stretching and Breaking of Ultrathin MoS2. ACS Nano 2011, 5 (12), 9703−9709.
(49) Akinwande, D.; Brennan, C. J.; Bunch, J. S.; Egberts, P.; Felts, J. R.; Gao, H.; Huang, R.; Kim, J.-S.; Li, T.; Li, Y. A Review on Mechanics and Mechanical Properties of 2D Materials—Graphene and Beyond. Extreme Mechanics Letters 2017, 13, 42−77.
(50) Fu, L.; Wan, Y.; Tang, N.; Ding, Y.-m.; Gao, J.; Yu, J.; Guan, H.; Zhang, K.; Wang, W.; Zhang, C. K-Λ Crossover Transition in the Conduction Band of Monolayer MoS2 under Hydrostatic Pressure. Science advances 2017, 3 (11), No. e1700162.
(51) Michail, A.; Parthenios, J.; Anestopoulos, D.; Galiotis, C.; Christian, M.; Ortolani, L.; Morandi, V.; Papagelis, K. Controllable, Eco-Friendly, Synthesis of Highly Crystalline 2D-MoS2 and Clarification of the Role of Growth-Induced Strain. 2D Mater. 2018, 5 (3), 035035.

(52) Giannozzi, P.; Baroni, S.; Bonini, N.; Calandra, M.; Car, R.; Cavazzoni, C.; Ceresoli, D.; Chiarotti, G. L.; Cococcioni, M.; Dabo, I. QUANTUM ESPRESSO: A Modular and Open-Source Software Project for Quantum Simulations of Materials. J. Phys.: Condens. Matter 2009, 21 (39), 395502.
(53) Giannozzi, P.; Andreussi, O.; Brumme, T.; Bunau, O.; Nardelli, M. B.; Calandra, M.; Car, R.; Cavazzoni, C.; Ceresoli, D.; Cococcioni, M. Advanced Capabilities for Materials Modelling with Quantum ESPRESSO. J. Phys.: Condens. Matter 2017, 29 (46), 465901.
(54) Perdew, J. P.; Burke, K.; Ernzerhof, M. Generalized Gradient Approximation Made Simple. Phys. Rev. Lett. 1996, 77 (18), 3865.
(55) Vanderbilt, D. Soft Self-Consistent Pseudopotentials in a Generalized Eigenvalue Formalism. Phys. Rev. B: Condens. Matter Mater. Phys. 1990, 41 (11), 7892.

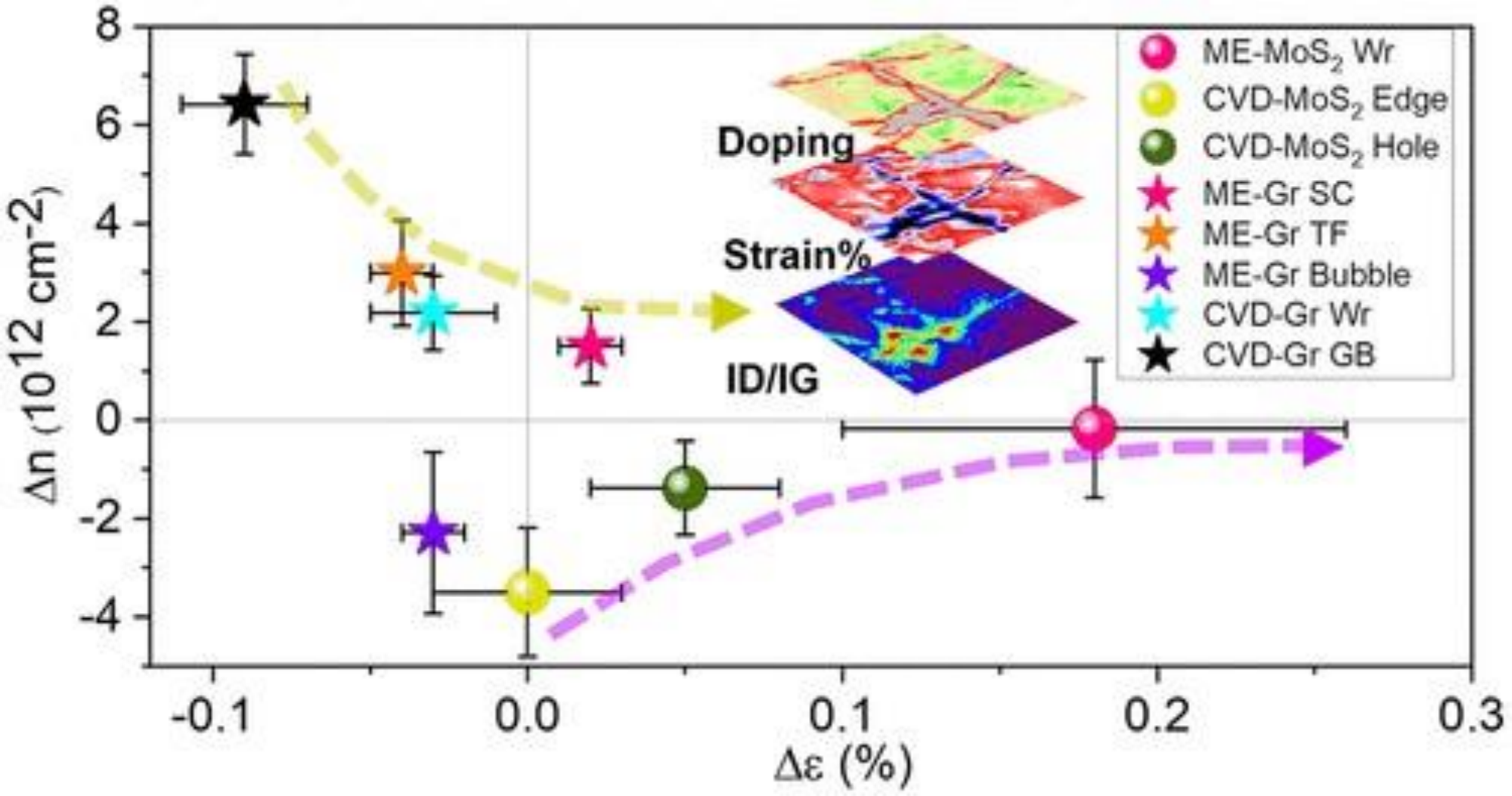
ME-MoS2 Wr
CVD-MoS2 Edge
CVD-MoS2 Hole
ME-Gr SC
ME-Gr TF
ME-Gr Bubble
CVD-Gr Wr
CVD-Gr GB
Doping
Strain%
ID/IG
Δn (10^12 cm^-2)
Δε (%)
8
6
4
2
0
-2
-4
-0.1
0.0
0.1
0.2
0.3

Supplementary Materials

Structural Defects Modulate Electronic and Nanomechanical Properties of 2D Materials

Manoj Tripathi[1#]*, Frank Lee[1#], Antonios Michail[2,3], Dimitris Anestopoulos[3], James McHugh[4], Sean P. Ogilvie[1], Matthew J. Large[1], Aline Amorim Graf[1], Peter J. Lynch[1], John Parthenios[3], Konstantinos

Papagelis[3,5], Soumyabrata Roy[6], Md. Abid S. R. Saadi[6], M. M. Rahman[6], Nicola Maria Pugno[7,8] , Alice A. K. King[1], P. M. Ajayan[6]*, Alan B. Dalton[1]*

[1]Department of Physics and Astronomy, University of Sussex, Brighton BN1 9RH, United Kingdom

[2] Department of Physics, University of Patras, Patras GR26504, Greece

[3] Institute of Chemical Engineering Sciences, Foundation for Research and Technology- Hellas (FORTH/ICE-HT), Patras GR26504, Greece

[4] Department of Chemistry, Loughborough University, Loughborough, LE11 3TU, United Kingdom

[5] School of Physics, Department of Solid State Physics, Aristotle University of Thessaloniki, Thessaloniki 54124, Greece

[6]Department of Materials Science and Nanoengineering, Rice University, Houston, Texas, 77005, United States

[7]Laboratory of Bio-Inspired and Graphene Nanomechanics, Department of Civil, Environmental and Mechanical Engineering, University of Trento, Via Mesiano 77, I-38123, Trento, Italy

[8]School of Engineering and Materials Science, Queen Mary University of London, London, E1 4NS, United Kingdom

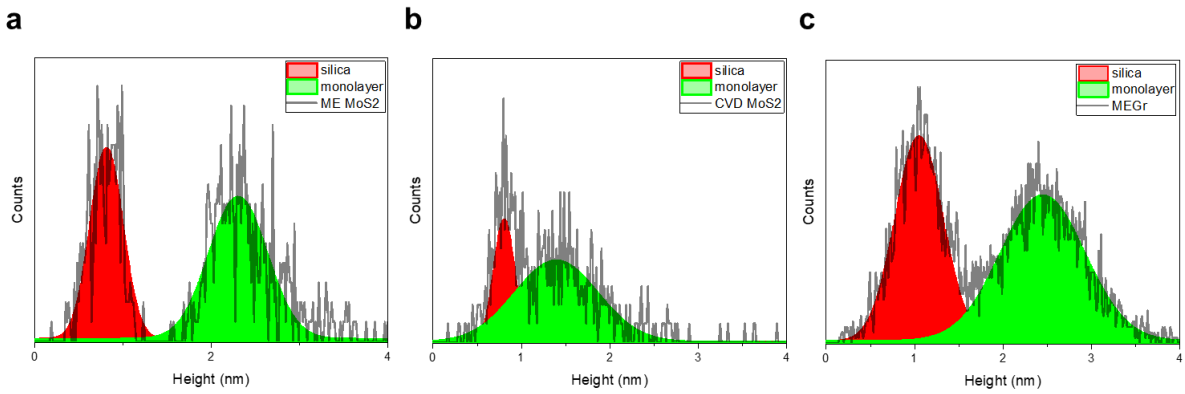
a
b
c
silica
monolayer
ME MoS2
CVD MoS2
MEGr
Counts
Height (nm)
0
1
2
3
4

Figure S1: The thickness analysis of (a) ME-MoS_2, (b) CVD-MoS_2 and (c) ME-Gr. By constructing a histogram of all the topographic data of silica and the monolayer in their interface region, we observe two peaks whose peak separation can be regarded as the thickness of the 2D material and it is found to be 0.93 ± 0.20 nm, 0.60 ± 0.40 nm, and 1.42 ± 0.55 nm for ME-MoS_2, CVD-MoS_2 and ME-Gr respectively. The thickness of all material falls into the range of monolayer.

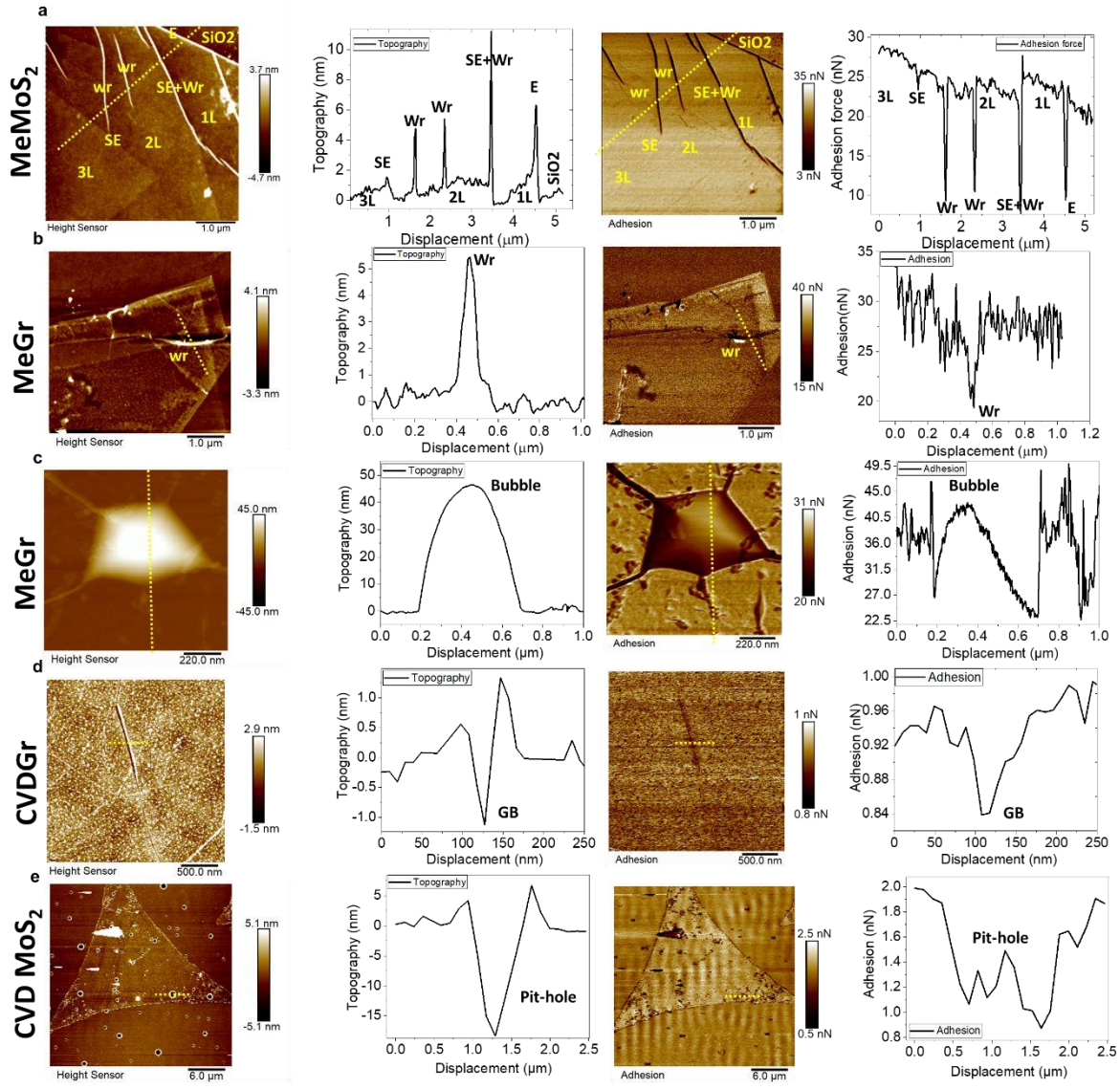
a
MeMoS2
SiO2
wr
wr
SE+Wr
1L
SE
2L
3L
3.7 nm
-4.7 nm
Height Sensor
1.0 μm
Topography
Topography (nm)
SE
Wr
Wr
SE+Wr
E
3L
2L
1L
SiO2
Displacement (μm)
SiO2
wr
wr
SE+Wr
1L
SE
2L
3L
35 nN
3 nN
Adhesion
1.0 μm
Adhesion force
Adhesion force (nN)
3L
SE
2L
1L
Wr
Wr
SE+Wr
E
Displacement (μm)
b
MeGr
wr
4.1 nm
-3.3 nm
Height Sensor
1.0 μm
Topography
Wr
Topography (nm)
Displacement (μm)
wr
40 nN
15 nN
Adhesion
1.0 μm
Adhesion
Adhesion(nN)
Wr
Displacement (μm)
c
MeGr
45.0 nm
-45.0 nm
Height Sensor
220.0 nm
Topography
Bubble
Topography (nm)
Displacement (μm)
31 nN
20 nN
Adhesion
220.0 nm
Adhesion
Bubble
Adhesion (nN)
Displacement (μm)
d
CVDGr
2.9 nm
-1.5 nm
Height Sensor
500.0 nm
Topography
Topography (nm)
GB
Displacement (nm)
1 nN
0.8 nN
Adhesion
500.0 nm
Adhesion
Adhesion (nN)
GB
Displacement (nm)
e
CVD MoS2
5.1 nm
-5.1 nm
Height Sensor
6.0 μm
Topography
Topography (nm)
Pit-hole
Displacement (μm)
2.5 nN
0.5 nN
Adhesion
6.0 μm
Adhesion
Adhesion (nN)
Pit-hole
Displacement (μm)

Figure S2: AFM topography and adhesion force map of nanoscale structural defects. (a) ME-MoS_2 showing wrinkles, step edge and edges. (b) ME-Gr showing a wrinkle up to a height of 5 nm. (c) inflated ME-Gr bubble up to a height of 45 nm. (d) Grain boundary (GB) of CVD-Gr showing an interface region between two grains. (e) Pit-hole in MoS_2 with a depth of 17 nm.

The adhesion force map is the work done carried by the tip apex to move away from the surface. Thus, it indicates the surface chemistry which influences the interfacial adhesion (pull-out) force between tip apex

(hydrophilic in present case). We observed a local drop in adhesion force at the structural defects as compared to its surrounding DF regions. Therefore, these structural defects are expected to show a hydrophobic behaviour as compared to its surrounding flat defect-free (DF) surface. It is worthy to note that the pull-out measurement is carried out by force-distance spectroscopy which is influenced by the relative humidity (33% in the present case), contact area, force applied and the nature of the subsurface.

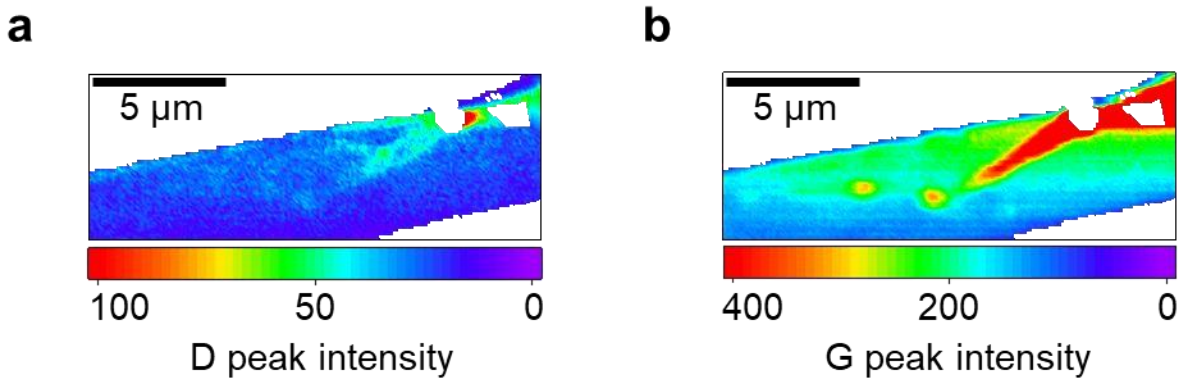
a
5 μm
100
50
0
D peak intensity
b
5 μm
400
200
0
G peak intensity

Figure S3: (a) The D peak intensity and (b) G peak intensity of the ME-Gr wrinkles in the same region as Fig 2c. Along the defect-free region to the wrinkles, D peak intensity rises from 20 to 70 while G peak intensity rises significantly more, from 40 to 400.

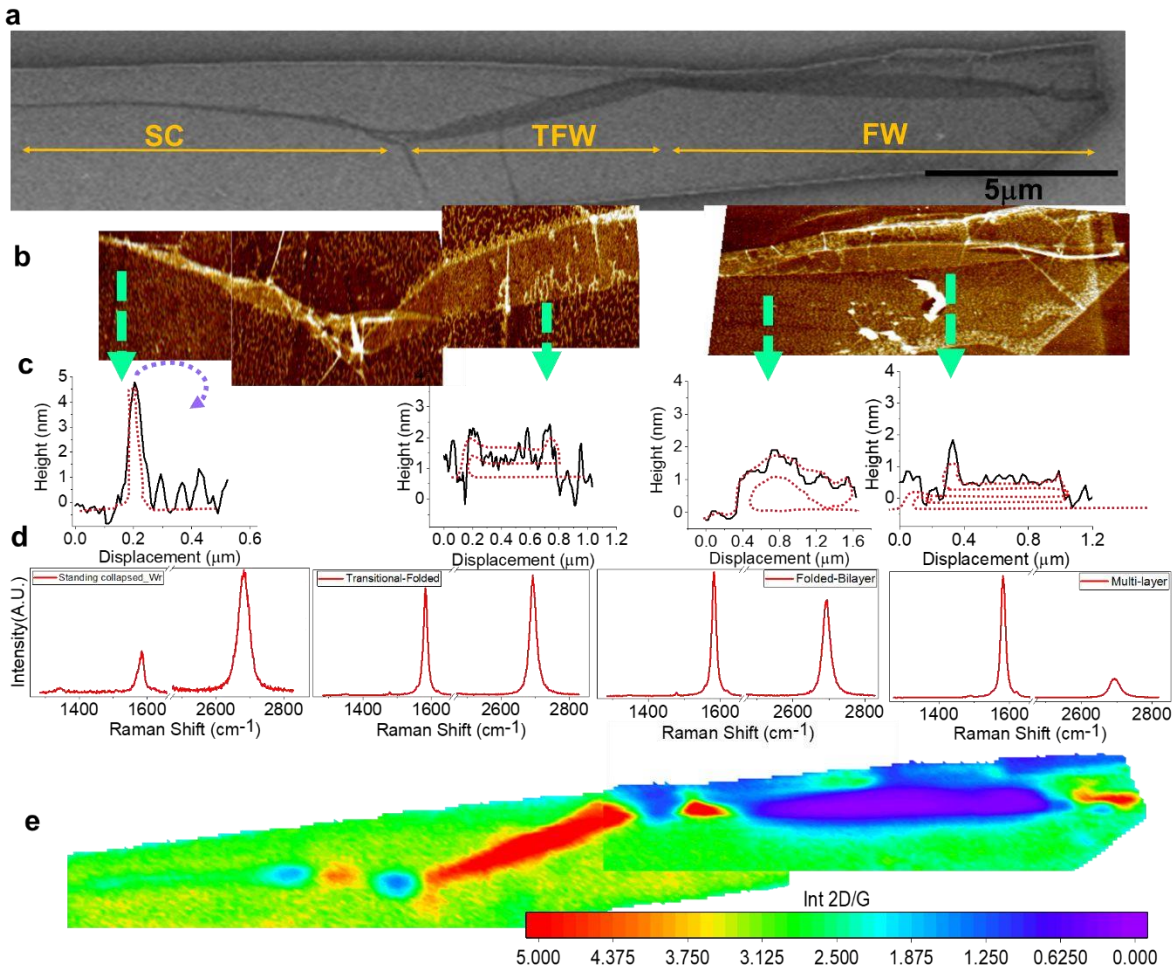
a
SC
TFW
FW
5μm
b
c
Height (nm)
Displacement (μm)
d
Intensity(A.U.)
Standing collapsed_Wr
Transitional-Folded
Folded-Bilayer
Multi-layer
Raman Shift (cm-1)
e
Int 2D/G
5.000
4.375
3.750
3.125
2.500
1.875
1.250
0.6250
0.000

Figure S4: Different geometries of a wrinkle in graphene. (a) SEM micrograph of single layer graphene illustrates transformation of wrinkle into different geometries: standing collapsed (SC), transitional-folded wrinkle (TFW) and multi-layered folded wrinkles (FW). (b) AFM images of wrinkles illustrate different height and width for SC, TFW and FW stages. (c) The line profile of a SC shows a height up to 4.5 nm; inset shows the predicted shape of the wrinkle based on the AFM profile. The curved arrow at SC wrinkle represents the bending direction of the wrinkle to form a transitional state of folded wrinkle of height up to 2 nm with broader width (approx. 600 nm) where each layer of the graphene might not couple to each

other. At the multi-layered folded configuration two possible structures are predicted as coupling of two graphene layers (height between 1-2 nm) and more than two layers (height up to 1 nm). There is a systematic decrease in the height of the wrinkles from SC to FW which indicates the decrease in spacing between the graphene layers. (d) Raman spectra of SC, TFW and FW graphene wrinkles with varying G intensity of the Raman mode with decreasing height of the wrinkles. (e) Raman map of an intensity ratio (2D/G) Raman modes of DF graphene and wrinkled region shows the distribution of single layer graphene with 2D/G > 1. SC and TFW wrinkles showing 2D/G intensity ratio > 1 might be due to less coupling

between the graphene layers in TFW. At FW region, the intensity ratio 2D/G < 1 indicates the coupling of graphene layers as validated from the AFM profile.

Figure S5: Raman mapping of polycrystalline graphene of an area of 10x10 □m^2 showing (a) higher intensity

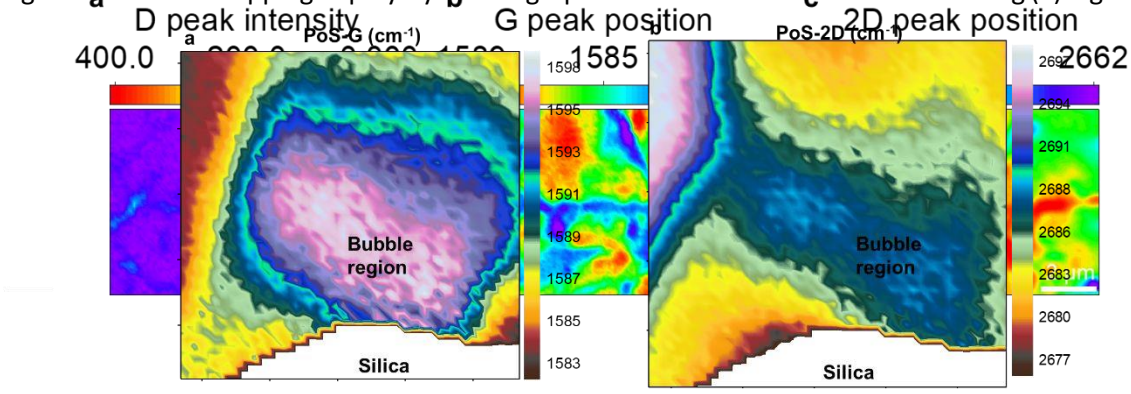

of D-peak distribution over wrinkles, (b) Pos(G) and (c) Pos(2D). The high D-peak intensity from the lines are showing blue shift in the Pos(G) and Pos(2D).

Figure S6: Raman mapping of 6-bubble region showing shift in G peak position (a) and 2D peak position (b). The bubble region shows redshift in Pos(G) and blue shift in Pos(2D) as compared to the surrounding defect free region (yellow color).

S7: *Calculation of strain and doping from Raman modes in Graphene and MoS_2*

The strain *(ε)* and the charge carrier concentration (*n)* of MoS_2 and graphene are related to the Raman shift (ω_1, ω_2) as presented in equation (1).[1-2]

$$\begin{pmatrix} \omega_1 \end{pmatrix} \quad \begin{pmatrix} \varepsilon \end{pmatrix}$$

$$\omega = T\ n \qquad (1)$$

where

$$\begin{pmatrix} -2\gamma_1\omega_{01} \\ k_1 \end{pmatrix}$$

$$T = -2\gamma_2\omega_{02}\, k_2 \qquad (2)$$

γ is the Grüneisen parameter, k is the doping shift rate and ω^o is the no-strain and no-doping peak position. The subscript denotes the corresponding Raman modes. In MoS_2 system, ω_1 numeric *(1)* and ω_2 *(2)* corresponds to the frequencies of E^1_{2g} and A_{1g}, respectively, while $\gamma_{E^1_{2g}} = 0.86$, $\gamma_{A_{1g}} = 0.15$,[3] $k_{E^1_{2g}} = -0.33 \times 10^{-13}\ cm^{-1}$, and $k_{A_{1g}} = -2.22 \times 10^{-13}\ cm^{-1}$.[4] As for graphene, ω_1 subscript *(1)* and ω_2 *(2)* are G and 2D modes respectively, where $\gamma_G = 1.95$, $\gamma_{2D} = 3.15$, $k_G = -1.407 \times 10^{-12}\ cm^{-1}$ and $k_{2D} = -0.285 \times 10^{-12}\ cm^{-1}$.[1, 5] In fact, the vector space of Raman peak positions ω_1-ω_2 is a linear transformation from the - space, while the origin of both spaces defines the absence of strain and doping. $\varepsilon\ n$ Therefore, ω represents the deviation of the recorded frequency from ω^0 due to strain or doping. It is to be noted that *n* represents the relative shift in the charge carrier and mostly originates from the charge exchange with the substrate. Also, the airborne impurities adsorb over the surface and at edge region may influence *n*. Using equation *(1)*; the correlation plot of Raman modes with contour lines representing isostrain and isodoping can be drawn for characterising local contribution of structural defects to strain and doping as compared to the DF region in the monolayer. Conversely, this influence can be more explicitly studied by strain and doping maps in virtue of an inverse transformation as presented in equation *(3).*

$$\begin{pmatrix} \varepsilon \\ n \end{pmatrix} = T^{-1}\begin{pmatrix} \omega_1 - \omega_{01} \\ \omega_2 - \omega_{02} \end{pmatrix} = \frac{1}{-2\gamma_1\omega_{01}\, 2\gamma_2\omega_{02}\, k_1 k_2} \begin{pmatrix} -2\gamma_2\omega_{02} & -k_1 \\ -k_2 & -2\gamma_1\omega_{01} \end{pmatrix} \begin{pmatrix} \omega_1 - \omega_{01} \\ \omega_2 - \omega_{02} \end{pmatrix} \qquad (3)$$

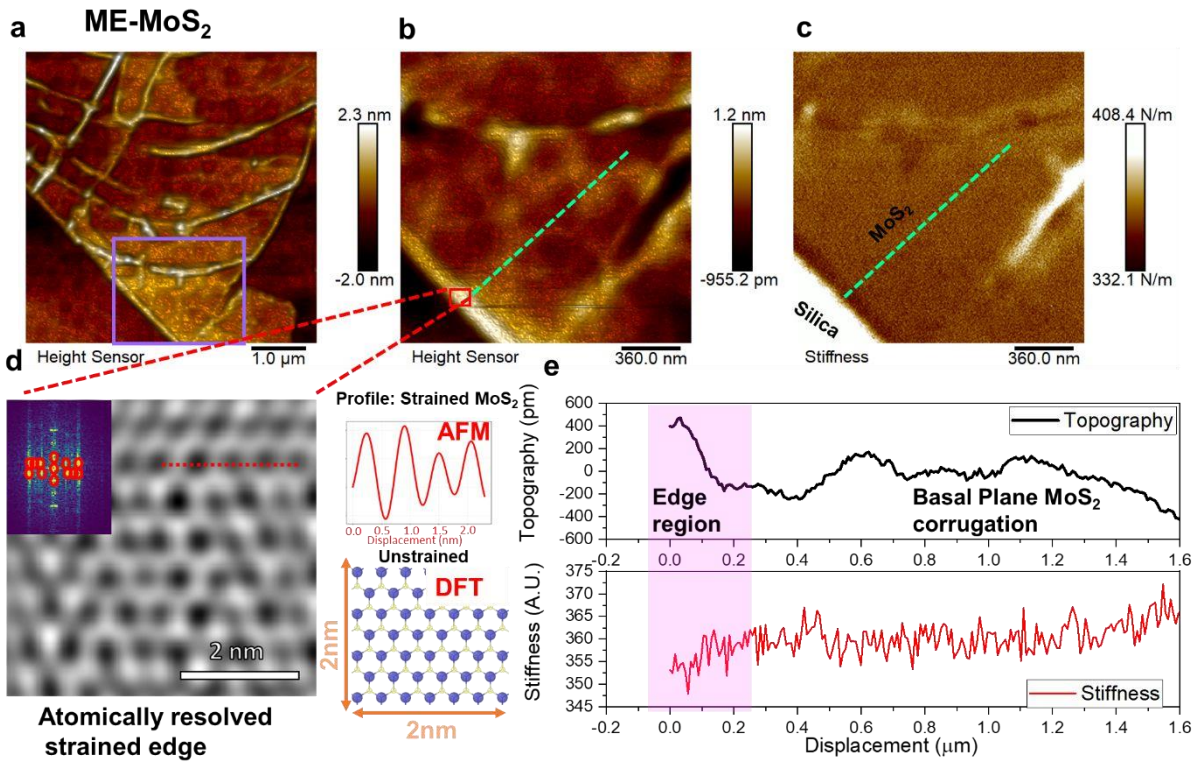

Figure S8: Characteristics of edge region of an atomic ME-MoS_2 relative to its DF basal plane: (a) 3D AFM topography of ME-MoS_2 illustrating edge, wrinkles and basal plain. (b) High-resolution 3D map of region marked in panel (a) illustrating different conformation of edge region and basal plane region. (c) The stiffness map of the same region as in panel (b). (d) FFT treated atomically resolved strained MoS_2 edge. The deviation in the hexagonal lattice point in FFT (inset) indicates strained atomic configuration of edge atoms. It is further validated through comparing with unstrained MoS_2 of an area of 2x2 nm^2 from DFT study and a line profile from AFM data reveals stretching of the lattice atoms of MoS_2. (e) Topographic profile of dashed line in panel (b) reveals corrugation of 1L MoS_2 where edge region is elevated (out-ofplane distortion) as compared to basal plane region. There is a drop in relative stiffness at the edge region as compared to the basal plane region. All these topographical and mechanical characteristics of MoS_2 edge atoms indicates relaxation mechanism of the edge atoms achieved through releasing the compressive strain from the basal plane.

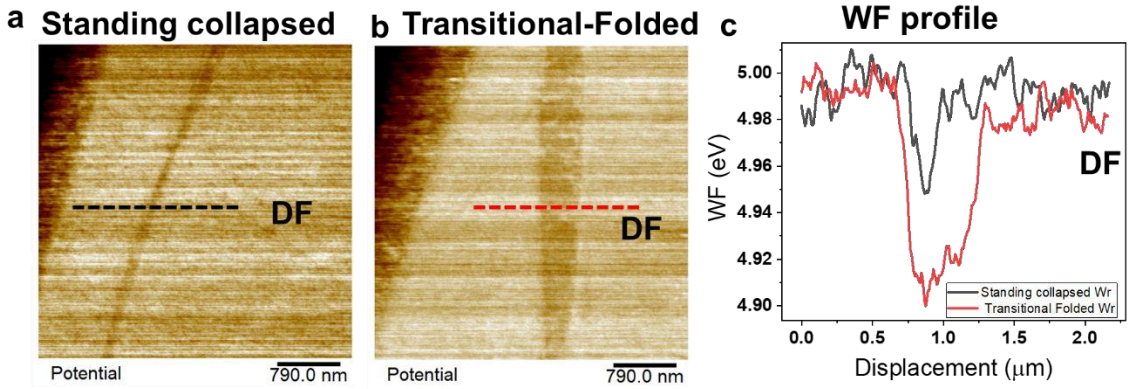

Figure S9: Surface potential map of wrinkled graphene. (a) Contact potential difference map of standing collapsed wrinkle graphene on silica. (b) Contact potential difference map of transitional-folded wrinkle showing broader region lower surface potential. (c) The work function (WF) line profile from CPD map shows a drop in the work function at the wrinkle. The transitional folded wrinkle shows broader area and lower in WF indicating higher carrier concentration due to altered geometry and its different coupling with substrate.

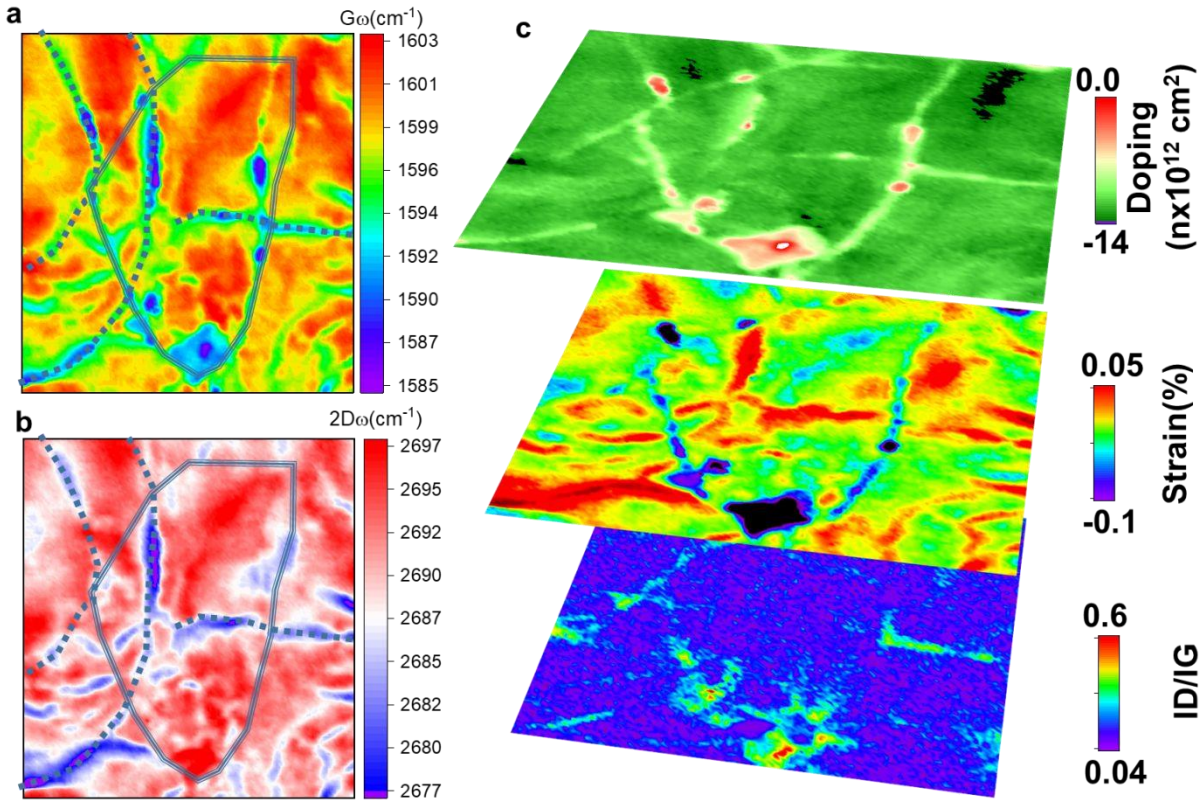

Figure S10: Raman mapping of CVD graphene of lateral size (10x10 μm^2), which has a domain grain boundary (contour drawn by a solid line), ripples (dashed line) and wrinkles (dashed line). (a) There is redshift in Pos(G) along the domain grain boundary and over wrinkles. (b) The Pos(2D) at the grain boundary is showing blueshift at the majority region and redshift over wrinkles/ripples (white and blue region). (c) There is high carrier concentration along the grain boundary; at the junction (interaction between wrinkle and grain boundary) carrier concentration (*n*) are observed highest among the entire CVD region. Compressive strain (-ε %) is prevailing at the grain boundary; wrinkles/ripples are showing tensile strain as compared to the surrounded flat region. The ratio of I_D/I_G shows the distribution of Raman active disordered structure along the grain boundaries and wrinkles. The I_D/I_G values are the highest at the intersection of wrinkles and grain boundaries.

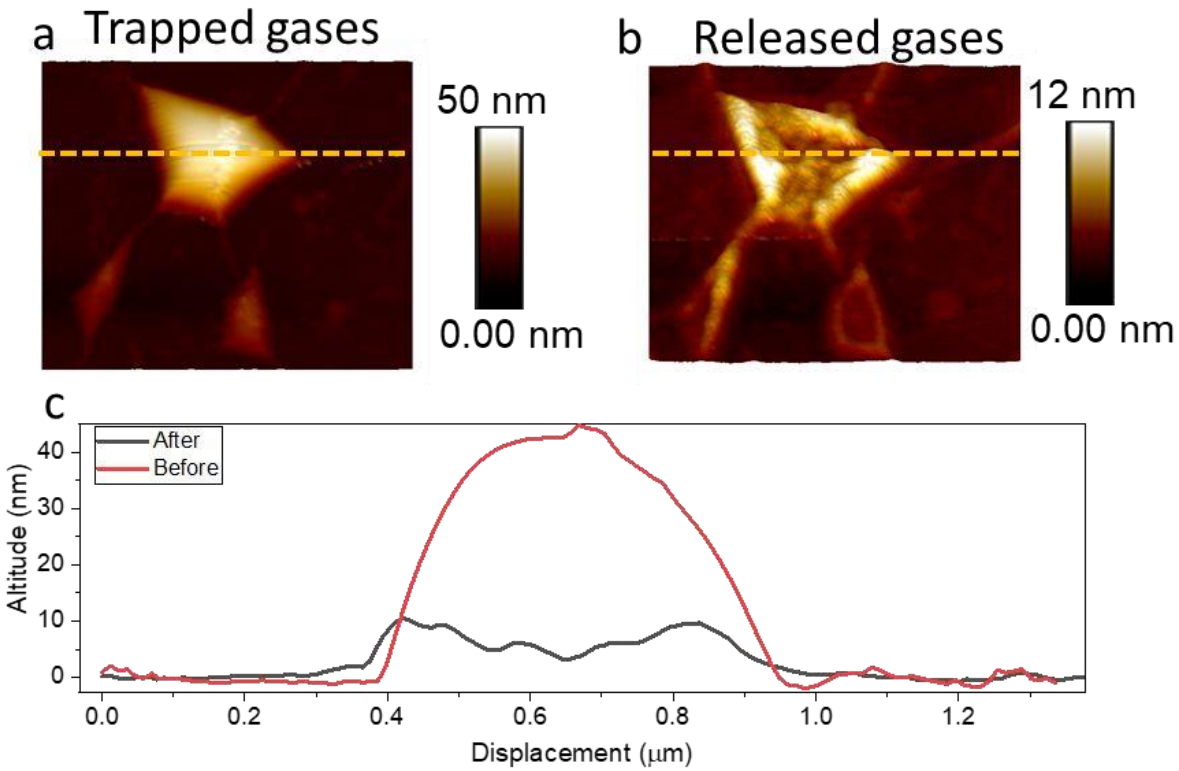

Figure S11: The 3D-AFM image of the same pentagonal pyramid graphene bubble (a) with trapped gases and (b) after the release of gases. The pentagonal shape generated due to formation of ridges in this geometry, which allows some relaxation of strain, and consequently a decrease in elastic energy. The trapped gases inflated the graphene and bulged out to an amplitude up to 45 nm and can induce tensile strain in the structure as compared to the flat graphene. The release of gases deflated the bubble structure causing it to collapse (amplitude 7.2 nm) down to the substrate, which can induce substrate compressive strain. Using the AFM profile, the perimeter (P) of the inflated (Po = 956.7 nm) and deflated (P = 600 nm) of an individual bubble are calculated and strain (ε_{AFM}) has been measured through relation (Po-P)/Po. We observed significant compressive strain (ε_{AFM} = -0.37%) in the deflated bubble as compared to the inflated bubble due to the reduction in perimeter length by 62% and slightly tensile strain (ε_{AFM} = 0.08%) as compared to surrounding flat graphene.

Table S1: Relative values of strain and doping from surrounding DF in MoS_2 and graphene.

MoS_2		Δε (%)	Δn (× 10^{12} cm^{-2})	**Graphene**		Δε (%)	Δn (× 10^{12} cm^{-2})
ME	Wrinkles	0.18 ± 0.08	-0.18 ± 1.40	ME	SC wrinkles	0.02 ± 0.01	1.50 ± 0.76
					TF wrinkles	-0.04 ± 0.01	2.99 ± 1.07
					Bubble	-0.03 ± 0.01	-2.29 ± 1.64
CVD	Edge	0.00 ± 0.03	-3.50 ± 1.31	CVD	Wrinkles	-0.03 ± 0.02	2.18 ± 0.75
	Pit-hole	0.05 ± 0.03	-1.38 ± 0.95		GB	-0.09 ± 0.02	6.42 ± 1.02

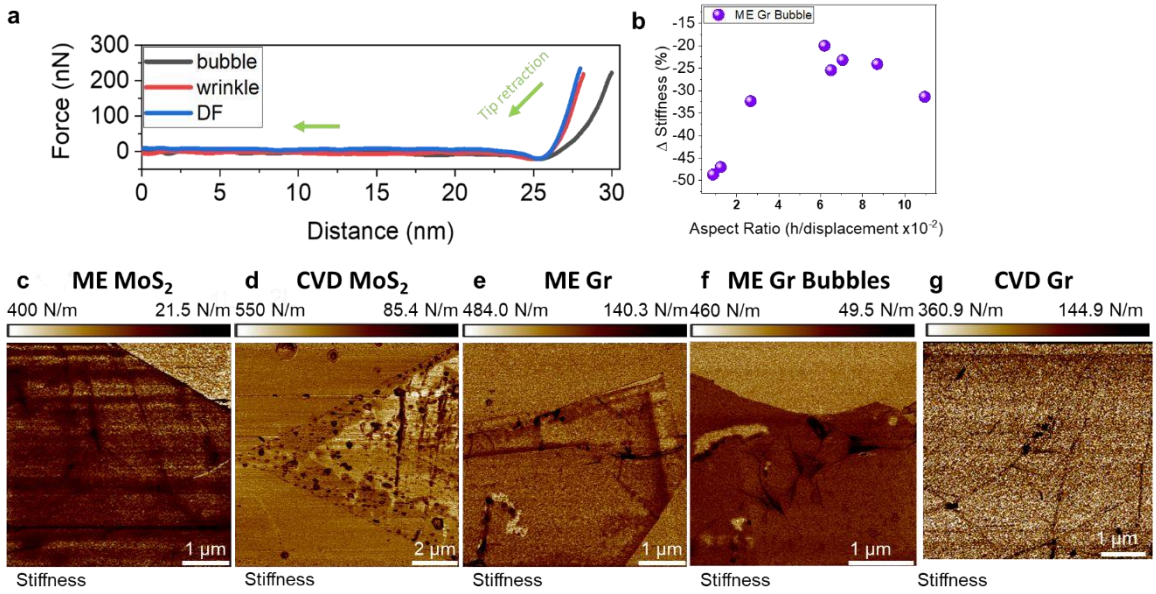

Figure S12: **The contact stiffness measurement of structural defects** (a) AFM force-distance retraction curve of ME graphene nanobubbles and wrinkles. The slope between 25 nm and 30 nm denotes the stiffness. (b) Variation in the normalized stiffness as a function of the aspect ratio of graphene bubble; the least drop in stiffness is showing aspect ratio of 6, which is associated with the trigonal and pentagonal shaped bubble. (c) The stiffness map of ME MoS_2 wrinkles and edges, (d) CVD MoS_2 holes and edges, (e) ME graphene wrinkles and edges, (f) ME graphene nanobubbles, (g) CVD graphene wrinkles.

The stiffness measurement is carried out by force-distance spectroscopy under the elastic limit of deformation. The cantilever applies pressure and deflection (□, nm) measured related to deformation of the samples. The values of the stiffness (N/m) measured by the linear-fit of the retraction part of force-distance spectroscopy (ref. 50 at main text). The measurements were performed at the structural defects and its surrounding DF region in a single acquisition to induce similar pressure at both regions. The reduction of stiffness values is observed for all defects as compared to surrounded DF. The elastic stiffness of each structural defect was carried out by controlled AFM force-distance curves of the retraction part as shown in **Figure S12a**. The x-axis represents the separation of the tip from its idle position that the tip retracts from approximately 29 nm to the origin, while the slope of the inclined section depicts the stiffness of the material. Repeated acquisition over the same region as in our previous measurements enables the construction of stiffness mapping of different defects, which are illustrated in **Figure S12 (c-g)**.

During force-distance spectroscopy, it is to be noticed that vertical separation for DF 2D materials to the underlying silica substrate is nearly 0.35 nm for graphene and 0.7 nm for MoS_2; thus, indentation up to 5 nm includes influence from the underlying substrate. In order to keep contact mechanics conditions similar that include the elastic deformation of thin 2D material and silica substrate, the same cantilever is used for the stiffness measurement. The indentation depth lies less than 10% of the 300 nm oxide layer of silica and higher than the roughness (rms= 0.22 - 0.40 nm) of the 2D layers, which are feasible conditions

to measure the elastic deformation. We did not observe any wear in the tip and to the substrate under this applied pressure.

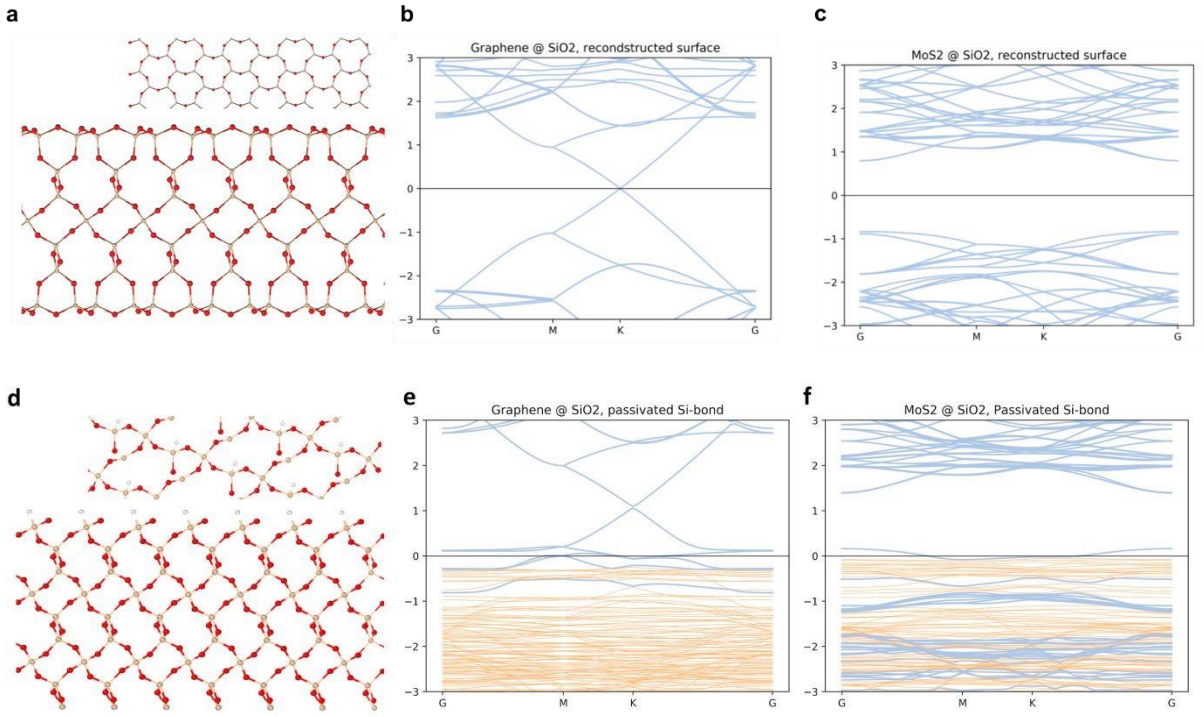

Figure S13: DFT simulations of monolayer-substrate interaction have been approximated using α-quartz SiO_2 with different surface terminations. Monolayers of graphene and MoS_2 have been placed above different surface terminations and full structural relaxations have been performed. (a) Top and side view of the fully-reconstructed SiO_2 surface, where Si and O can be found along the surface bond with one another leaving no dangling bonds. Both graphene and MoS_2 exhibit a weak binding (0.051, 0.06 eV/atom, respectively) and a larger equilibrium distance for this termination. (b) Band diagrams of graphene and (c) MoS_2 on the reconstructed surface, demonstrating that the electronic structure of both monolayers is effectively unchanged. (d) α-quartz SiO_2 with hydrogenated Si bonds and dangling O bonds. The dangling oxygen bonds induce a stronger interaction with the substrate (0.1, 0.3 eV/atom for graphene and MoS_2, respectively (e) Band diagrams of graphene and (f) MoS_2 on the O-terminated surface. Monolayer bands are shown in blue while substrate bands are coloured orange. Our simulations demonstrate the movement of the Fermi level into the conduction bands for both graphene and MoS_2 which is indicative of p-doping of the monolayer by the exposed oxygen bonds at the substrate surface.

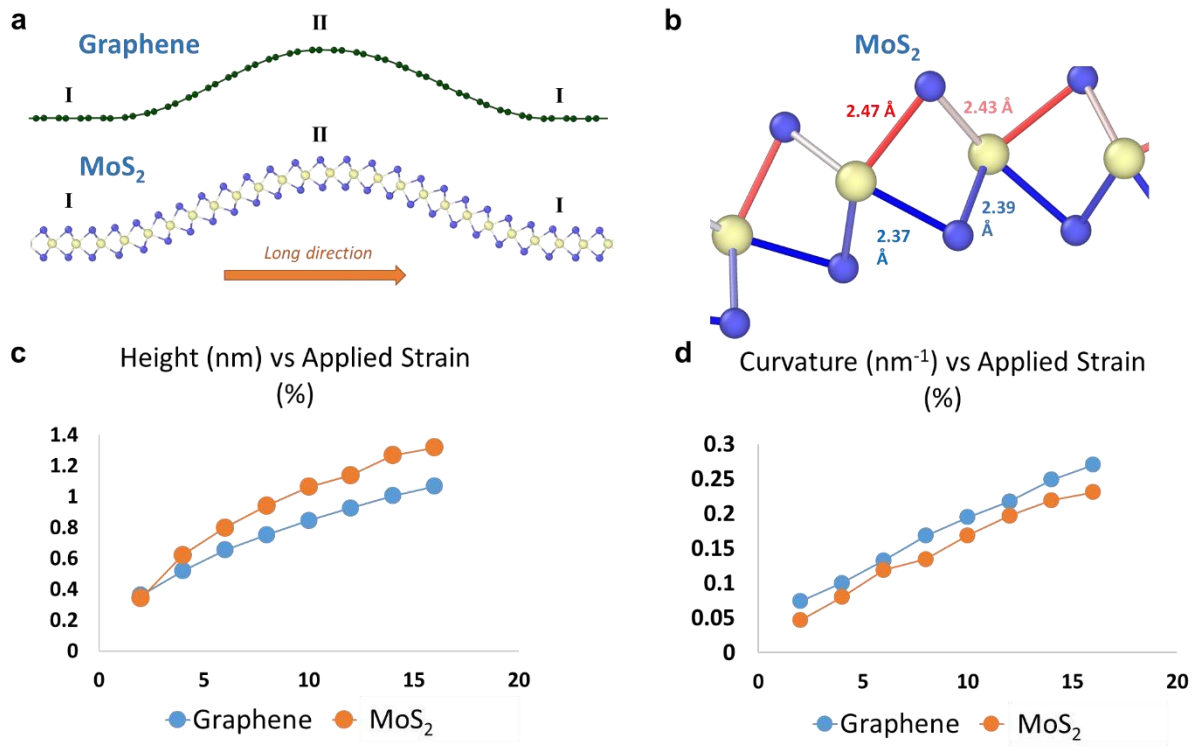

Figure S14: DFT Simulations of rippled graphene and MoS_2 monolayers. (a) Periodic arrangement of the unit cells in graphene and MoS_2 in armchair configuration as flat and rippled geometry. Compressive strain is applied to the unit cell in the direction of pointed arrow. Atoms in the region I are constrained to remain flat by constraining forces to the in-plane directions, while those in region II are allowed to freely relax, inducing out-of-plane buckling to release the strain. (b) The implementation of lateral strain results in asymmetric bond distortion due to the finite width of MoS_2 as compared to graphene. (c) Final height and (d) total curvature across a ripple after structural optimization. The height is taken as the difference of the out of plane coordinate between the flat DF region and the ripple peak, while the net curvature across a ripple is calculated as $C = H/W^2$, where W (taken as the full width at half maximum across the ripple) and H are the width and height respectively.

S15: In the following we provide some brief notes on our DFT simulations of graphene wrinkles. Similarly to our MoS_2 simulations, which show different strain trends due to difference in the orientation of bonds with respect to the globally applied and local strains, we find that the degree of bond compression depends on the orientation of the bond with respect to the applied strain. This is shown schematically in **Figure S15(a)**.

In order to compare our simulations results to the experiment, we have performed relaxations of wrinkled cells with different boundary conditions in the flat region. For one set of simulations, only in-plane relaxation is allowed in region I (free conditions), while a second set of simulations were performed where region I was fixed at the perfect graphene lattice constant (fixed conditions). Nevertheless, we do not find that these conditions greatly impact the relaxed height and structural parameters of the wrinkles, they do affect the bond lengths upon full relaxation. This is shown in **Figure S15(b)** for the ripple of equilibrium height 1.6 nm.

In the fixed case, the bond length in region I remains constant, while under free conditions there is a moderate reduction due to net compression. Across the ripple, the strain accommodation is tensile in the case of fixed conditions, while for Free relaxation the bond lengths are compressive in comparison to the surrounding flat material. In both cases, the bond lengths across the fully relaxed ripple are similar. The main distinction between the two cases lies in the fact that when the surrounding flat regions are fixed at the perfect lattice constant, all compressive strain accommodation occurs at the ripple, and this region is then under a comparative compression. When the atoms in region I are also allowed to relax, strain is now accommodated in both regions and the wrinkled region II is under a small tension with respect to the flat, compressed region I.

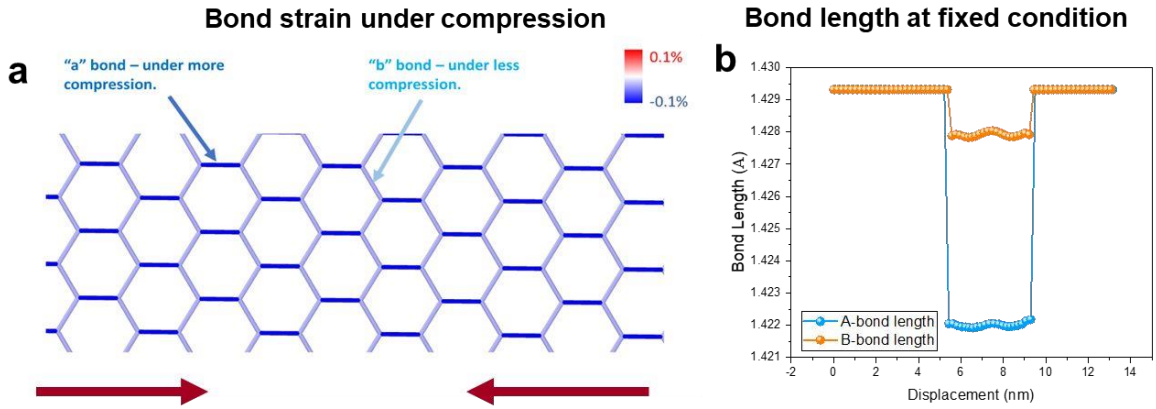

Figure S15: (a) Bond compression for a graphene sheet under a small applied strain. "a" bonds lie parallel to the applied strain and therefore experience a larger degree of bond compression, while "b" bonds have a large component which is perpendicular to the strain and therefore undergo a smaller degree of compression. (b) Variation in the lengths of the A and B bonds upon structural relaxation for the fixed boundary conditions.

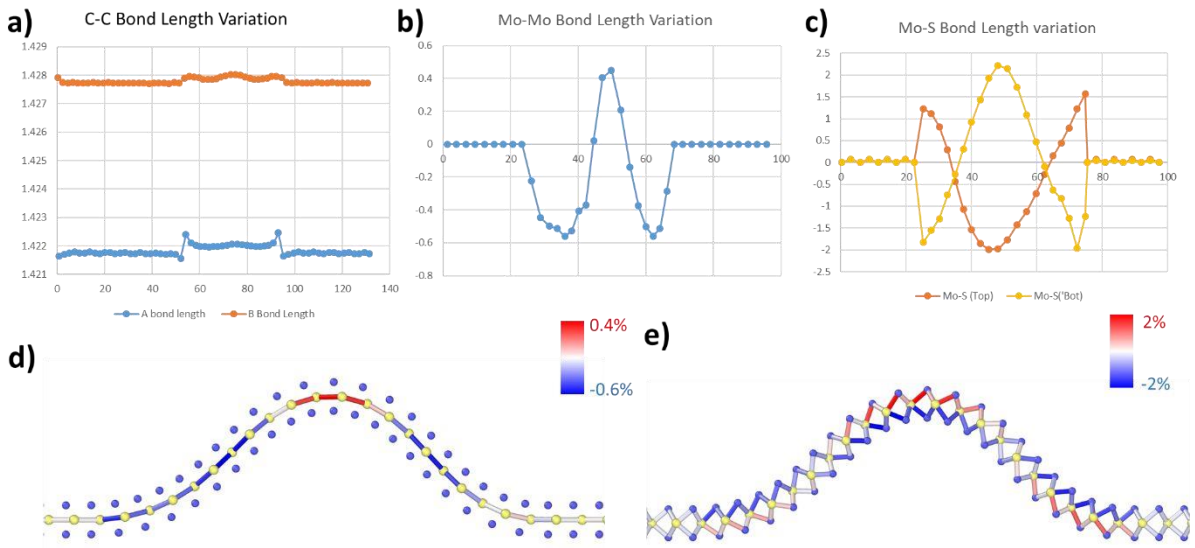

Figure S16: Bond strain in rippled graphene and MoS_2 monolayers. (a) Variation in total bond length of laterally strained carbon-carbon bonds across a 1 nm height graphene ripple. (b) Variation in Mo-Mo and (c) Mo-S bonds across a 1 nm height MoS_2 ripple. Both the Mo-Mo and Mo-S bonds show substantially larger variation than the graphene carbon bonds (d) Mo-Mo bond lengths coloured according to bond strain and (e) Mo-S bond length variation for the 1 nm MoS_2 ripple. The Mo-S bond depends both on the ripple height and relative orientation of the Mo and S layers.

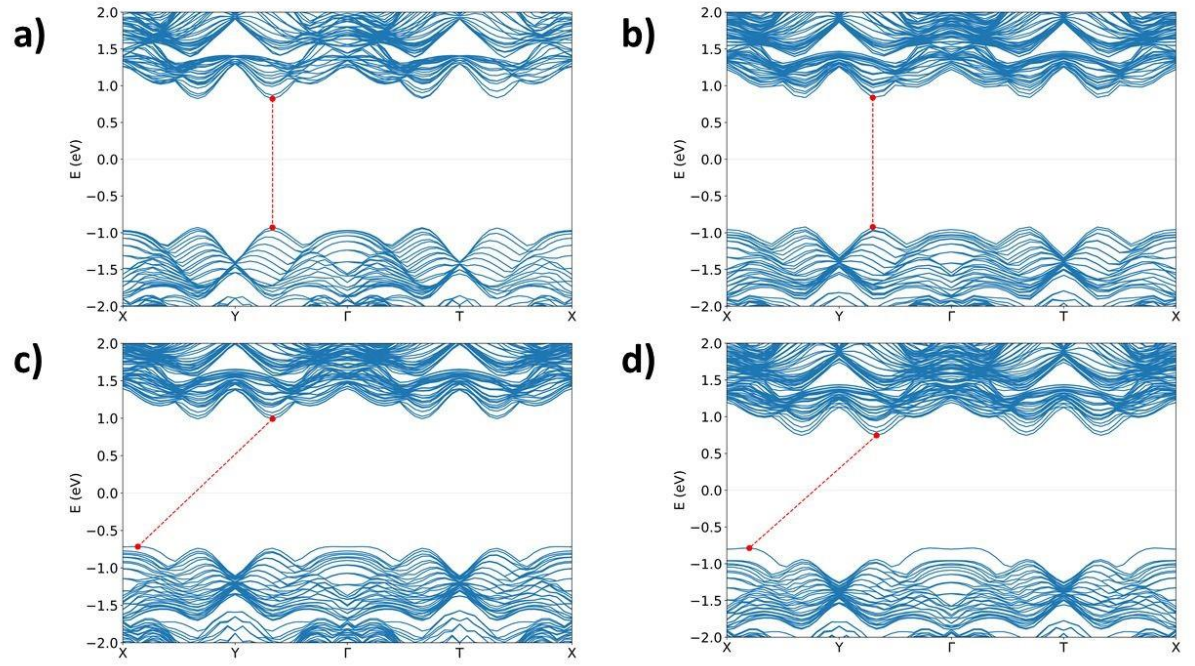

Figure S17: MoS_2 band structures with increasing ripple curvature, for final ripple heights (a) 0.342 nm, (b) 0.890 nm, (c) 1.138 nm, (d) 1.318 nm. With increasing strain, the rippled MoS_2 transitions from a direct gap semiconductor to an indirect gap semiconductor.

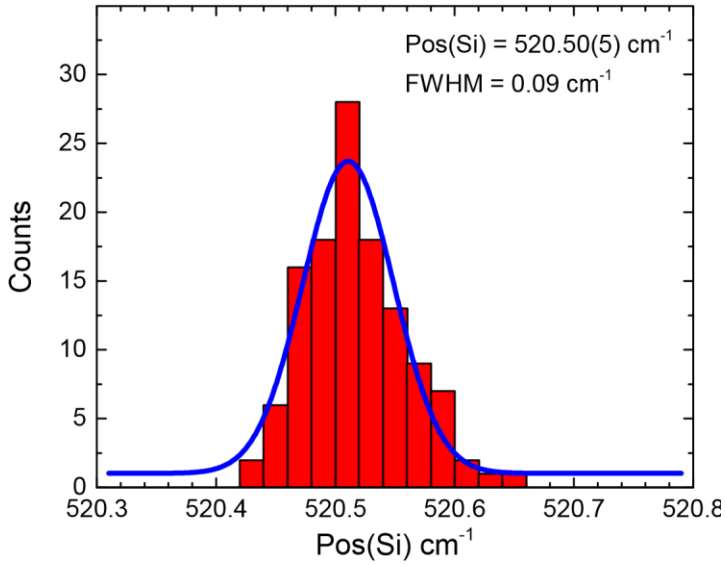

Figure S18: Determining spectral accuracy using Si wafer as reference. Raman spectroscopy has been carried out over Si wafer to obtain 121 spectra, which are then fitted with Lorentzian to estimate the peak position. The average value is measured as 520.514 ± 0.015 cm^{-1}, revealing a good spectral accuracy.

In order to determine the spectral accuracy of our system, a total number of 121 Raman spectra were collected from a single spot of a reference Si crystal. The Si Raman peak (~520.5 cm^{-1}) was fitted with a Lorentzian lineshape. The histogram of the fitted peak centres is presented in Figure S18 above. The FWHM of the distribution is 0.090 cm^{-1} (standard deviation = 0.045 cm^{-1}) and the error in the determination of the peak position by the fitting procedure is 0.015 cm^{-1}. For MoS_2, the uncertainties for the E^1_{2g} and A_{1g} modes are 0.22 cm^{-1} and 0.047 cm^{-1}, respectively. Therefore, the spectral accuracy of the Raman system is below
0.1 cm^{-1}, which is adequate to track the change of E^1_{2g} and A_{1g} peaks in a step of 0.6 cm^{-1}.

References:

1. Lee, J. E.; Ahn, G.; Shim, J.; Lee, Y. S.; Ryu, S., Optical Separation of Mechanical Strain from Charge Doping in Graphene. *Nature Communications* **2012,** *3*.
2. Michail, A.; Delikoukos, N.; Parthenios, J.; Galiotis, C.; Papagelis, K., Optical Detection of Strain and Doping Inhomogeneities in Single Layer MoS2. *Applied Physics Letters* **2016,** *108* (17).
3. Rice, C.; Young, R. J.; Zan, R.; Bangert, U.; Wolverson, D.; Georgiou, T.; Jalil, R.; Novoselov, K. S., Raman-Scattering Measurements and First-Principles Calculations of Strain-Induced Phonon Shifts in Monolayer MoS2. *Physical Review B* **2013,** *87* (8).
4. Chakraborty, B.; Bera, A.; Muthu, D. V. S.; Bhowmick, S.; Waghmare, U. V.; Sood, A. K., SymmetryDependent Phonon Renormalization in Monolayer MoS2 Transistor. *Physical Review B* **2012,** *85* (16).

5. Jiang, T.; Wang, Z.; Ruan, X.; Zhu, Y., Equi-Biaxial Compressive Strain in Graphene: Grüneisen Parameter and Buckling Ridges. *2D Materials* **2018,** *6* (1), 015026.